

# Assessing Atmospheric Moisture Effects on Heavy Precipitation During the HyMeX IOP16 Using GPS Nudging and Dynamical Downscaling

Alberto Caldas-Alvarez<sup>1</sup>, Samiro Khodayar<sup>1,2</sup>

5 <sup>1</sup>Institute of Meteorology and Climate Research (IMK-TRO), Karlsruhe Institute of Technology, Karlsruhe, P.O. Box, 76131, Germany

<sup>2</sup>Mediterranean Centre for Environmental Studies (CEAM), Valencia, 46980, Spain

*Correspondence to:* Alberto Caldas-Alvarez (alberto.caldas-alvarez@kit.edu)

**Abstract.** Gaining insight on the interaction between atmospheric moisture and convection is determinant to improve the model representation of heavy precipitation, a weather phenomenon that every year brings casualties and monetary losses in the western Mediterranean region. Given the large variability of atmospheric moisture, an accurate representation of its distribution is expected to reduce the errors related to the representation of moist convective processes. In this study, we use a diagnostic approach to assess the sensitivity of convective precipitation and underlying mechanisms during a heavy precipitation event (Hydrological cycle in the Mediterranean eXperiment; HyMeX Intensive Observation Period; IOP 16) to variations of the atmospheric moisture spatio-temporal distribution. Sensitivity experiments are carried out by nudging a homogenised data set of Global Positioning System-derived Zenith Total Delays (GPS-ZTD) with sub-hourly frequency (10 minutes) in 7 km and 2.8 km simulations with the Consortium for Small scale Modelling in CLimate Mode (COSMOCLM) model over the western Mediterranean region. The analysis shows that (a) large atmospheric moisture amounts (Integrated Water Vapour; IWV ~ 40 mm) precede heavy precipitation at the affected areas. This occurs 12 h prior to initiation over southern France and 4 h over Sardinia, north eastern Italy and Corsica, which is our main study area. (b) We found that the moisture is swept from the Atlantic by a westerly large-scale front associated with an upper-level low on the one hand and evaporated from the Mediterranean Sea and north Africa on the other. The latter moisture transport occurs in the <1 km to 4 km layer and has been identified for this event for the first time. (c) COSMO-CLM overestimated the atmospheric humidity over the study region (Corsica) and this was, to a good extent, corrected by the GPS-ZTD nudging. This reduced drastically maximum precipitation (- 49 % for 7 km and -16 % for 2.8 km) considerably improving the precipitation representation in the 7 km. The convection permitting simulation (2.8 km) without the GPS-ZTD nudging already did a good job in representing the precipitation amount. (d) The two processes that exerted the largest control on precipitation reduction were the decrease of atmospheric instability over the island (Convective Available Potential Energy; CAPE -35 %) and the drying of the lower free troposphere bringing additional dry air entrainment. Besides, the 7 km simulation showed a weakening of the represented low-pressure system and the associated cyclonic wind circulation. This reduced ultimately, the intensity and number of convective

updrafts represented over the island. These results highlight the large impact exerted by moisture corrections on precipitating convection and the chain of processes leading to it across scales.

## 1 Introduction

35 Heavy precipitating convection causes yearly serious damages and casualties in countries of the Western Mediterranean (WMed) basin especially by autumn (Llasat et al., 2010; Gilabert and Llasat, 2017). During these events, daily accumulated precipitation over 150 mm is not rare and precipitation rates can be well over 20 mm h<sup>-1</sup> (Ducrocq et al., 2014; Röhner et al., 2016). These are caused mainly by convective events ranging several temporal and spatial scales, from the mesoscale down to the micro-alpha (Ducrocq et al., 2016; Funatsu et al., 2018). Accurate representation of the convective processes is crucial to support forecasters and decision makers to prevent impacts on properties and communities. The WMed is especially prone to  
40 heavy precipitating convection by autumn because of the combination of the relatively high sea surface temperature of the Mediterranean and the Atlantic, the arrival of low-pressure systems such as extra-tropical cyclones or upper-level troughs and the interaction with the Mediterranean complex orography (Ducrocq et al., 2014). Atmospheric moisture plays a decisive role at all phases of convective development and therefore it is relevant to gain knowledge on moist convective processes to improve the modelling of extreme phenomena (Sherwood et al., 2010; Ahrens and Samson, 2010). Given the high spatio-temporal  
45 variability of atmospheric moisture (Steinke et al., 2015; Girolamo et al., 2016), a deficient representation of its distribution has been pointed out as a source of uncertainty in current predictions (Chazette et al., 2015; Khodayar et al., 2016). That is why, there is growing interest in developing forecast systems that assimilate humidity observations with sub-hourly frequency (Guerova et al., 2016). Given the novelty of such assimilation frequencies and the multiple methodologies applied, new insights are needed on their impact on simulated atmospheric conditions leading to heavy precipitation.

50 Determinant for the heaviest precipitation events in the WMed are the vast moisture amounts which may originate from remote or local sources (Ricard et al., 2012; Krichak et al., 2014; Khodayar et al., 2016). Depending on the synoptic conditions, the Mediterranean Sea can account for over 50 % of the transported moisture (Duffourg and Ducrocq, 2011). This is the case when an anticyclonic flow dominates the 3 to 4 days preceding heavy precipitation. Remote sources such as the Atlantic and the tropics also supply the needed moisture, especially for the heaviest precipitation events (Pinto et al., 2013; Winschall et al.,  
55 2014), whose transport is brought via tropical plumes (Chazette et al., 2015b) or extra-tropical cyclones (Xoplaki et al., 2012). Finally, north Africa has been also identified as a source by Duffourg and Ducrocq (2011). Regions prone to convective development are correlated with areas of moisture convergence where building up of conditional instability takes place (Ricard et al., 2012; Khodayar et al., 2016). Given the correlation between the location of moisture convergence and precipitating convection, the complex Mediterranean orography plays a decisive role in setting areas prone to heavy precipitation. The high  
60 mountain ridges constrain the moisture transports in the basin favouring moisture gathering at the mountain foothills, the coasts and the valleys. Moreover, the elevated terrain provides dynamic lifting to the convergent moist air masses triggering convection.

In addition to the moisture transport, the variability and stratification determine when, where and how intense, convection can be. Several studies (Duffourg and Ducrocq, 2011; Ricard et al., 2012; Khodayar et al., 2016, Maranan et al., 2019) have highlighted the moistening of the lower troposphere as a necessary factor for precipitating convection to develop with specific humidity values up to  $10 \text{ g kg}^{-1}$  below 850 hPa. A moist low-level, increases the Convective Available Potential Energy (CAPE) of the lifted parcel. A second factor, crucial for convection intensity is the moisture at the Lower Free Troposphere (LFT). This is the moisture transport that occurs above the Planetary Boundary Layer (PBL). Recent observational studies (Virman et al., 2018; Schiro and Neelin, 2019) concluded that the probability of intense convection increases rapidly with increasing LFT humidity, especially over land. Whether this sensitivity of heavy precipitation to LFT moisture variations is well represented by current atmospheric models has been investigated by past sensitivity modelling studies using fine model resolutions, from  $\Delta x \sim 500 \text{ m}$  to  $\Delta x \sim 7 \text{ km}$  (Keil et al., 2008; Honda and Kawano, 2015; Lee et al., 2018). They demonstrated that convection enhancing (weakening) happened with increasing (diminishing) moisture at the LFT in the simulations. These studies performed moisture sensitivity experiments modifying the water vapour distribution by adding or subtracting a prescribed water vapour amount at chosen heights. It is thus, of particular interest to investigate the aforementioned issues by performing corrections toward observations instead of using idealized experiments.

A powerful technique to correct the atmospheric moisture distribution is Data Assimilation (DA). Recent advances in remote sensing techniques for atmospheric moisture and the growing computational power have enabled the achievement of relevant improvements for heavy precipitation representation (Wulfmeyer et al., 2015). A well-established method to assimilate data is the Nudging scheme. Nudging consists of relaxing the model's prognostic variables towards measurements (Schraff and Hess, 2012), where the main advantages are its simplicity (Guerova et al., 2016) and that it has shown good results especially in analysing humidity fields as compared to other schemes (Schraff et al., 2016). Nudging can be used to assimilate Global Positioning System (GPS) measurements that provide information on the total column atmospheric moisture. The demonstrated benefits of using GPS measurements are that it is an all-weather product (as opposite to other remote sensing integrated products), its large accuracy and its high temporal resolution (Cress et al., 2012; Guerova et al., 2016). The GPS data set used for nudging in this work is provided in the framework of the Hydrological Cycle in the Mediterranean Experiment (HyMeX; Ducrocq et al. 2014), which is particularly unique given the common processing of data from more than 25 European networks its dense coverage and its frequency of five minutes (Bock et al., 2016).

Our study focuses on the Intensive Observation Period (IOP) 16 of the HyMeX field campaign in autumn 2012 (Ducrocq et al., 2014) taking Corsica as our study region. The event was selected due to the combination of propitious instability and moisture conditions interacting with the Corsican complex orography. It has been also selected given the large impact shown to GPS nudging in seasonal simulations of the complete autumn 2012 period performed in our working group. This on-going work revealed that the GPS nudging was able to reduce the existing wet bias in the model with a non-systematic response for heavy precipitation. HyMeX IOP16 was highlighted as one of the events where the GPS nudging was beneficial to reduce the precipitation overestimation.

Within this framework, this work is devoted to assess the sensitivity of convective precipitation and underlying mechanisms to variations of the atmospheric moisture spatio-temporal distribution. Our objectives are 1) to gain knowledge on the role of local and remote atmospheric moisture contributions to the convection-related processes leading to the occurrence of the event, 2) to assess the model sensitivity to continuous GPS nudging and 3) to quantify the impact of the GPS nudging depending on the model resolution.

The organization of the paper is as follows. Section 2 describes the model experiments and presents the observational data sets used for model validation and nudging. Section 3 provides a description of the event including the synoptic situation, the convective evolution and the transport of moisture. Section 4 discusses the impact of the GPS nudging in precipitation, humidity and convective-related processes and Sect. 5 presents the conclusions.

## 2.1 Observations

### *GPS-Zenith Total Delay*

The Zenith Total Delay (ZTD) is the “excess path length of GPS satellite emissions (in the L1 and L2-band) caused by the refractivity of the neutral atmosphere” (Businger et al., 1996). The refractivity definition for the neutral atmosphere depends on the partial pressures of water vapour and dry air and on the temperature as introduced in ground papers of GPS meteorology (Bevis et al., 1994). The ZTD is proportional to the Integrated Water Vapour (IWV) in the zenith direction. The ZTD is given in length units and the delay in the Zenith direction is usually preferred given it shows the shortest delays. It is obtained from the slanted path delays by means of mapping functions,  $Z_m(\theta)$  dependent on the curvature of the Earth and the elevation angle (Duan et al., 1996). The dataset used for the sensitivity experiments, is provided by the Laboratoire de Recherche en Géodésie (LAREG) and the HyMeX community and its specifications can be found in Bock et al. (2016). It merges data from more than 900 stations with 20 stations over Corsica, our study region, is made available in temporal resolutions up to five minutes and it has a dense coverage of the western European countries (see Fig. 1). All networks have been commonly processed by the GIPSY-OASIS II software to guarantee homogeneity. Data screening includes outliers, range and ambiguity checks to increase the accuracy. The comparison against radiosonde IWV measurements has shown no significant biases during night-time and biases in the range 0.5 – 1.4 mm during daytime (Bock et al., 2016).

### *Radiosondes*

In the framework of the HyMeX SOP1 MétéoFrance provides the operational soundings containing more than 30 atmospheric parameters, including temperature, dew point temperature, geopotential height, air pressure, wind direction and horizontal wind speed. In average, they contain ca. 30 levels between the surface and the 300 hPa level with about one measurement every 250 m. In addition to the operational soundings, supplementary soundings were launched during the HyMeX IOPs. Hence, the temporal resolution of the soundings lies between 12 h and 6 h. In total, 10 stations are used among which 3 (Gibraltar, Mallorca and Dar El Beïda) are used for process-understanding and 7 over the Italian Peninsula, Croatia, Corsica and Sardinia are used for validation of the specific humidity and IWV simulations. We perform the validation of the model

130 data obtaining the nearest grid points to the location of the radiosondes. No height correction is applied for this purpose since  
135 the difference in height between the neighbouring grid points and the height of the radiosonde stations does not exceed 30 m  
in any case. The data is accessible at [http://mistrals.sedoo.fr/?editDatsId=595&datsId=595&project\\_name=HyMeX](http://mistrals.sedoo.fr/?editDatsId=595&datsId=595&project_name=HyMeX).

#### *Rain gauges*

Météo-France and the HyMeX program provide the HyMeX domain precipitation amount (Nuret, 2013; SEDOO OMP. doi:  
135 10.6096/mistrals-hymex.904) data set with hourly accumulated precipitation measured by rain gauges. Over 5000 stations are  
deployed over the WMed land parts with about 30 stations placed over the island of Corsica. The version used (V4) enjoys the  
newest quality control and checks for double stations. The data set spans the Sep-2012 to Mar-2013 period.

#### *The NOAA CPC Morphing Precipitation (CMORPH)*

140 CMORPH makes available precipitation measurements in a rectangular grid merging satellite microwave observations. These  
are combined using the Morphing technique (Joyce et al., 2004, <https://doi.org/10.5065/D60R9MF6>), that uses motion vectors,  
derived from infrared data to transport the microwave information to spots where no microwave data were available. It has a  
broad coverage (60°S - 60°N), and its spatial and temporal resolution at the equator is of 8 km and 30 minutes. The Climate  
Prediction Center (CPC) of the National Weather Service (NWS) in the USA provides the data and it spans the period 1998 to  
145 2015. CMORPH has shown a good detection skill in validation studies (Bitew and Gebremichael, 2011; Habib et al., 2012)  
and high correlation rates with sub-daily rain gauge data (Sapiano and Arkin, 2009).

#### *Global Land Evaporation Amsterdam Model (GLEAM)*

GLEAM provides daily accumulated terrestrial evaporation (evapotranspiration) in a 0.25° x 0.25° grid, spanning the period  
150 2003-2017. GLEAM computes the total evaporation over land from the sum of bare-soil evaporation (Eb), transpiration (Et),  
open-water evaporation (Ew), Snow sublimation (Es), snow sublimation (Es) and interception loss (Ei), as described in  
Martens et al. (2017) and Miralles et al., (2011). Four interconnected modules dealing with the rainfall interception, soil stress,  
soil state and the evaporation calculation, compute the aforementioned contributions. The four modules are forced by gridded  
global data which, in the version used in this work (v3b), is obtained mostly from remote sensing products, such as the Clouds  
155 and the Earth's Radiant Energy System (CERES) for radiation, the Tropical Rainfall Measurement Mission (TRMM) for  
precipitation, the Atmospheric Infrared Sounder (AIRS) for air temperature or European Space Agency Climate Change  
Initiative Soil Moisture (ESA CCI SM) for soil moisture. GLEAM version v3b has shown an average correlation with in-situ  
measurements of 0.78. In the validation, only 2 out of 63 stations showed differences with a level of significance of 10 %  
(Martens et al., 2017).

160

#### *The Hybrid Single-Particle Lagrangian Integrated Trajectory Model (HYSPLIT)*

The HYbrid Single-Particle Lagrangian Integrated Trajectory (HYSPLIT) computes air parcels, dispersion and chemical transformations (Stein et al., 2015; Rolph et al., 2017). In this paper, we use HYSPLIT to compute backward trajectories of moisture sources. The HYSPLIT model uses a hybrid approach combining lagrangian trajectories with the Eulerian methodology, using a fixed three-dimensional grid as a frame of reference (Stein et al., 2015). The free access internet-based platform READY (<https://www.ready.noaa.gov/index.php>) offers HYSPLIT trajectories calculation using eight different atmospheric model analyses of meteorological data. In this work, we use the half-degree archive of the National Centers for Environmental Prediction (NCEP) Global Data Assimilation System (GDAS) that spans the period 2007 to present and has a global coverage. The dataset is accessible in [https://www.ready.noaa.gov/HYSPLIT\\_traj.php](https://www.ready.noaa.gov/HYSPLIT_traj.php), last accessed 18-July-2019.

## 170 **2.2 The COSMO-CLM Model and the GPS-ZTD Nudging Sensitivity Experiments**

### **2.2.1 Consortium for Small-scale Modelling in Climate Mode (COSMO-CLM)**

The COSMO model is based on the fully compressible, nonhydrostatic, hydro-thermodynamical equations of the atmosphere. COSMO-CLM simulates the atmosphere as a multicomponent continuum constituted by, liquid water, dry air, water vapour and solid water in the form of cloud droplets ice crystals, raindrops, rimed aggregates, hail and graupel (Schättler et al., 2016). We use the COSMO version 5.00 in climate configuration. This implies that the slow-changing variables (ozone concentration, aerosol concentration and canopy variables) evolve in time. This brings a more realistic representation for seasonal simulations such as the ones presented in this work. The dynamic solver is a third order Runge-Kutta split-explicit scheme following Wicker and Skamarock (2002). It uses an Arakawa-C/Lorenz grid with scalars defined at the centre of the grid box and the normal velocity components defined on the corresponding box faces. The grid is rotated, and the height coordinate shows a Gal-Chen terrain-following grid stretching. The model uses a sponge layer with Rayleigh damping at the top boundary and three grid point lines for adaptation at the lateral boundaries. The boundary and initial states of the atmospheric prognostic variables are obtained by coarser resolution forcing models in a one-way nesting approach. The soil state and the surface-atmosphere interactions are simulated through the TERRA-Multi-Layer model (TERRA-ML; Doms et al., 2011). TERRA-ML has eight soil layers and is responsible for issuing the temperature and humidity conditions at the ground and considers the processes of evaporation, runoff, snow storage and interception storage. COSMO-CLM in the used resolutions of this work (7 km and 2.8 km), parameterizes the turbulent diffusion using a 1D diagnostic closure for the turbulent kinetic energy (Doms et al., 2011). The grid-scale clouds and precipitation are parameterized using a bulk scheme including several hydrometeor types (Doms et al., 2011). The radiation is parameterized following the formulation after Ritter and Geleyn (1992). In the case of grid spaces larger than 3 km sub-grid deep moist convection is parameterized using a mass-flux, low-level scheme with the equilibrium closure based on moisture convergence (Tiedtke, 1989). Shallow convection is parameterized using an adaptation of the Tiedtke scheme in the simulations using a 7 km and a 2.8 km grid.

### *The Nudging Scheme*

Following Schraff and Hess (2012), “nudging or Newtonian relaxation consists of relaxing the model’s prognostic variables towards prescribed values within a predetermined time window”. The extent of the relaxation depends on the difference between the observed and the modelled variable ( $\varphi_k^{obs} - \varphi(x_k, t)$ ), a weighting factor considering the measurement location and its representativeness ( $W_k(x, t)$ ) and a coefficient that modulates the impact of the analysis increments ( $G_\varphi$ ). This term is added to the result provided by the dynamics and numerics ( $F(\varphi, x, t)$ ). These terms define the state of the prognostic variable ( $\varphi(x, t)$ ) in the nudging equation (Eq. 1).

$$\frac{\partial}{\partial t} \varphi(x, t) = F(\varphi, x, t) + G_\varphi \cdot \sum_{k_{obs}} W_k(x, t) \cdot [\varphi_k^{obs} - \varphi(x_k, t)] \quad (1)$$

For any observation type, the weighting factor considers the spatial and temporal distance to the location of the observation by means of the horizontal ( $w_{xy}$ ), vertical ( $w_z$ ) and temporal weights ( $w_t$ ). The weight for spreading in the horizontal direction is a second-order autoregressive function dependent on the distance between the observation and the target point ( $\Delta r$ ) and the correlation scale ( $s$ ), see Eq. (2). This implies that the impact of the assimilated observation decreases with the distance to the station location. For example, the horizontal weight is halved ( $w_{xy} = 0.5$ ) at a distance of 135 km at the 500 hPa level.

$$w_{xy} = (1 + \Delta r/s) \cdot e^{-\Delta r/s} \quad (2)$$

The vertical interpolation of the observed data is performed assuming a Gaussian decay in height differences (Eq. 3). The vertical interpolation is also applied in the case of GPS-ZTD nudging since a profile of specific humidity is constructed from the derived GPS-IWV value. This constructed profile shall be treated by the nudging scheme as an upper-air measurement in the remainder of the process. The applied vertical weight (Eq. 3) depends on the distance between the height of the model level and the height of the observation ( $\Delta z = z - z_{obs}$ ), the virtual temperature at the height of the observation ( $T_v^{z_{obs}}$ ) and the correlation scale for humidity (0.2).

$$w_z = \exp\left\{-\left(\left(g/RT_v^{z_{obs}}\right) \cdot \Delta z/0.2\right)^2\right\} \quad (3)$$

Regarding temporal weighting, for hourly or even more frequent data measured from a stationary platform, the data are linearly interpolated to the model time. The observations are assigned to a grid point in the spatio-temporal space and the body of the report is evaluated. This is the step where gross error and consistency checks, quality control and redundancy checks dismiss suspicious observations.

In the case of GPS-ZTD observations, they are converted to IWV following Bevis et al. (1994). Making use of run-time COSMO-CLM pressure and temperature values linearly interpolated to the station location (Schraff and Hess, 2012). The observations are assigned to a grid point in the model space, provided the altitude difference of the GPS station and model surface lays within the range -150 to 600 m to allow for extrapolation and interpolation, respectively. Then they are converted to a specific humidity profile ( $q_v^{mod}$ ). given IWV is not a model prognostic variable as opposite to specific humidity. The profile is constructed by means of an iterative process that scales the observed IWV ( $IWV^{obs}$ ) with the modelled one ( $IWV^{mod}$ ) until a sufficiently low error is reached or alternatively after 20 iterations. Eq. (4) describes the iterative formula. The first

225 profile ( $q_{v_i}^{mod}$ ) used as the first guess for the iterative process, is the modelled specific humidity profile. Hence, the profile used for nudging depends on the vertical humidity distribution simulated by the model at the beginning of the nudging time-window.

$$q_{v_{i+1}}^{mod} = q_{v_i}^{mod} \cdot \frac{IWV^{obs}}{IWV_i^{mod}} \quad (4)$$

### 2.2.2 The GPS-ZTD Nudging Sensitivity Experiments

230 The Nudging scheme is used to assimilate GPS-ZTD data to assess the sensitivity of heavy precipitating convection to corrections of the spatio-temporal distribution of atmospheric moisture. We employ seasonal simulations of the autumn 2012 to profit from the full length of the GPS-ZTD data set.

The methodology is described as follows, we perform reference runs, hereafter referred to as CTRL, of the period 1-Sep 0000 UTC to 20-Nov 0000 UTC using two different horizontal resolutions (7 km and 2.8 km). Subsequently, we simulate the same period, keeping the same settings but nudging GPS-ZTD data continuously every 10 minutes. These runs are called NDG-7 and NDG-2.8. The 7 km runs (CTRL-7 and NDG-7) have been forced by European Centre for Medium-Range Weather Forecasts (ECMWF) analyses with a 6-hourly frequency. The 2.8 km runs (CTRL-2.8 and NDG-2.8) are forced by the CTRL-7 simulation in a one-way nesting strategy. CTRL-7 forces NDG-2.8 to ensure a fair comparison between CTRL-2.8 and NDG-2.8 with the same boundary and initial conditions. The simulation domains are contained in Fig. 1. We assimilate GPS data continuously to assess the differences in model representation from the free runs and the runs with an improved representation of the atmospheric column content. In this sense we a diagnostic approach and our experiments do not assess the impact of the assimilation on the subsequent first guess forecast.

240 Within the 80-day period of simulation, there were several events, largely affected by the GPS-ZTD nudging. IOP16, the case study of this paper, is especially interesting given the large reduction of maximum precipitation (-49 %) induced by the GPS-ZTD nudging over the investigation area of Corsica in the course of 26 h. The remaining cases of the autumn 2012 period and analyses on the complete season are part of a series of modelling studies from our working group, including a PhD thesis by Caldas-Alvarez (2019). IOP16 is also given the important role of the local orographic and instability factors in triggering and maintaining convection rather than the large-scale upper level forcing. We observed in the seasonal simulations that cases occurring under a weak synoptic forcing are more impacted by the GPS-ZTD nudging given the strong correction of the lower to middle tropospheric humidity. We validate the model output against in-situ humidity measurements quantifying the Mean Absolute Error (MAE) and Mean Bias (MB) and the Agreement Index (AI, see Eq. 3) adapted from González-Zamora et al. (2015). More details on these validation metrics can be found in the Annex. The precipitation fields are validated against rain gauges and the evapotranspiration over land using spatial averages of the GLEAM product.

255 To investigate the impact of moisture variations on convection-related processes, such as atmospheric latent and potential instability conditions, several convective related indices are examined. The CAPE, providing information about the latent instability, is obtained through the mean layer parcel method, as described in (Leuenberger et al., 2010). KO-index is obtained as the differences in Equivalent Potential Temperature ( $\theta_e$ ) between several levels of the atmosphere up to 500 hPa (Andersson



et al., 1989) hence it bears information on potential instability and how the upper-levels introduce atmospheric instability. Finally, the moisture flux is obtained by multiplying specific humidity and the horizontal wind following Ricard et al. (2012) but computed at each pressure level.

### 260 **3 Atmospheric Moisture transport and Precipitating Convection during IOP16**

During IOP16 several convective systems affected regions in the north-WMed and rain gauge stations measured totals up to 200 mm d<sup>-1</sup> over southern France, 150 mm d<sup>-1</sup> south of the western Alps and 250 mm d<sup>-1</sup> at the gulf of Genoa (250 mm d<sup>-1</sup>). Over Corsica, most precipitation occurred over the western side of the island for twelve hours, with maximum precipitation intensities reaching 25 mm h<sup>-1</sup>.

265 In this section, we use observations from radiosondes, the Evapotranspiration product GLEAM (see Sect. 2.1), CMORPH precipitation estimates, backward trajectories and the CTRL-7 simulation to understand the transport and distribution of moisture towards the WMed region. To validate the atmospheric moisture field of CTRL-7 we present in Table 1 the MAE, the AI and the MB of IWV between CTRL-7 and operational sounding measurements. In total, we selected 55 soundings from 7 stations (blue squares within the 2.8 km simulation domain in Fig. 1), during the period 26-Oct 0000 UTC to 28-Oct 0000  
270 UTC with a temporal resolution between 6 h and 12 h. CTRL-7 has a MAE of 2.7 mm, a MB of 0.61 mm and AI of 0.88. These values are within the acceptable range and are of the same order as the RMSE values found in other publications of IWV comparison between model data and GPS observations (Bock et al., 2016).

#### **3.1 Synoptic conditions**

The synoptic situation during the IOP16 was characterized by a cut-off low displacing westerly from the Iberian Peninsula  
275 toward southern France between 25-Oct 1200 UTC and 27-Oct 0000 UTC (Thévenot et al., 2015). The upper levels showed an associated diffluent flow with a south-westerly to southerly circulation at the low levels over the western part of the basin. Such a synoptic situation is prototypical for HPEs in the WMed (Jansa et al., 2001; Duffourg and Ducrocq, 2011). Over the Thyrreanean Sea on the morning of 26-Oct, the low-level flow induced convergence to the south of France. Figure 2 shows the geopotential height of the 500 hPa level (FI500), the Pressure at the Mean Sea Level (PMSL) and the spatial distribution of  $\theta_e$   
280 at 850 hPa at three hours of the event as represented by CTRL-7. Figure 2.a shows the situation on the 26-Oct 0600 UTC where values of  $\theta_e$  larger than 320 K take place. This moist and energetic southerly flow agrees with past publications referring values of the wet bulb temperature ( $\theta_w$ ) over 16 °C (Duffourg et al., 2016; Martinet et al., 2017). Six hours later (Fig. 2.b) the cut-off Low progressed toward the border of France and Spain further deepening. On the 26-Oct 1800 UTC, the high values of  $\theta_e$  (> 320 K) finally reached Corsica as well as extensive parts of the Thyrreanean Sea (see Fig. 2.c). Northerly cold winds  
285 terminated the event in the early morning of 27-Oct.

### 3.2 Convective evolution over Corsica

In the early morning of 26-Oct convection triggered and organized into a V-shape MCS close to the north-eastern coast of Spain. This MCS was named MCS0 by Thévenot et al. (2015) and hereafter we adopt the same nomenclature. This is shown by Fig. 3.a, depicting the convective cloud tops through brightness temperature images obtained with the Spinning Enhanced Visible Infrared Imager (SEVIRI) in a composite image at 0000 UTC, 0730 UTC and 1400 UTC. Northward, in the proximity of the Gulf of Lions, new convective cells triggered forming an MCS (MCS1) at 0500 UTC that would split into two defined MCSs (MCS1a and MCS1b). The two split MCSs moved toward southern France and eastward respectively in the course of 6 h (Duffourg et al., 2016). At the southern French region, the first MCS induced precipitation accumulations over 70 mm. South of the Alps, the second split MCS brought values over 90 mm (see Fig. 3.b, showing the accumulated precipitation between 26-Oct 1300 UTC and 27-Oct 1500 UTC for the whole WMed). Another MCS developed at the Liguria-Tuscany region in north-western Italy around 0730 UTC named MCS2 after Thévenot et al. (2015), not shown here. This area shows the highest precipitation rates of the event with over 245 mm in 24h (Duffourg et al., 2016). High convective cloud tops are also observed over the mid Mediterranean west of Corsica at 0730 UTC as shown by the brightness temperature (Fig. 3.a). This shows that convection is already happening offshore before the cells arrive at the island. At 1400 UTC over the island, the offshore convection is reinforced by orographic lifting of the moist low-level air masses.

Over Corsica, which is our study region, precipitation total values reach maximum accumulations between 75 mm and 100 mm, over the windward side of the mountains and over the mountain crests, between 50 mm and 75 mm (see Fig. 3.b). At the lee side of the mountain, the accumulated precipitation reaches 30 mm. The first convective cells occur over the island between 1300 UTC - 1500 UTC on the 26-Oct, forced by orographic lifting precipitating with intensities up to  $11.5 \text{ mm h}^{-1}$  over the windward side of the mountains (not shown). Between 26-Oct 1900 UTC and 27-Oct 0100 UTC, offshore convective systems arrive at the island (see Fig. 3.a). This stage has the largest precipitation intensities of the event (up to  $16 \text{ mm h}^{-1}$ , not shown) with precipitation falling mostly over the western part of the island, transitioning from the north at 2100 UTC to the south at 2300 UTC.

### 3.3 Atmospheric moisture transport

The transport of moisture feeding the convective systems at Corsica, southern France and north-eastern Italy arises from the action of the upper-level pressure low through two mechanisms. First, the associated front swept atmospheric moisture from the Atlantic to the Mediterranean in the course of 36 h. Second, from intense evaporation over the Mediterranean and north-Africa between 25-Oct 1800 UTC and 26-Oct 1200 UTC transported by the southwesterly flow. Figure 4 shows the CTRL-7 representation of IWV between 25-Oct 1200 UTC and 26-Oct 1200 UTC in the WMed at three hours with the simulated wind fields at 850 hPa. Given the overall good performance of CTRL-7 in representing IWV (Table 1) we use this simulation to study the moisture origins. At 25-Oct 1200 UTC (Fig. 4.a), the front associated with the pressure low west of the Iberian Peninsula carried large IWV amounts, up to 40 mm over the strait of Gibraltar and along the southern Portuguese coast. Local

areas at the Gulf of Lions (southern France) also showed values as large as 40 mm at about 12 h before precipitation initiation. At 26-Oct 0000 UTC, the Atlantic moisture is already located over the Algerian coast and at the Gulf of Lions (see Fig. 4.b).  
320 Along the Algerian coast, these high moisture amounts at 26-Oct 0000 UTC were a combination of moisture pushed by the low-pressure system from the Atlantic and moisture evaporated from north African land. The large moisture amount present at the Gulf of Lions originates partly from the Mediterranean Sea due to evaporation along the Spanish eastern coast, as introduced in Thevenot et al. (2015) and Martinet et al. (2017). At the hour of precipitation initiation over Corsica (26-Oct 1200 UTC), vast IWV amounts surrounded the western and southern coasts of the island (see Fig. 4.c). These large IWV values  
325 (~ 40 mm) surrounded the island 4 h prior to precipitation initiation. We have additionally validated these moisture transports against the Moderate Resolution Imaging Spectroradiometer (MODIS) daily product but we do not show it here given the presence of extensive cloud cover during the period hampering the quantitative validation. The visual comparison is included in the supplementary material (Fig. S.1).

To better assess the timing and vertical stratification of the moisture transport the time-height cross-sections of Equivalent  
330 Potential Temperature ( $\theta_e$ ), specific humidity and horizontal winds measured by radiosondes between 24-Oct and 27-Oct 0000 UTC at Gibraltar (Spain), Dar el Beïda (Algeria) and Mallorca (Spain) are shown in Fig. 5. The cross-section of Gibraltar (Fig. 5.a) shows high specific humidity values throughout the complete atmospheric column (3 g kg<sup>-1</sup> at 500 hPa and 11 g kg<sup>-1</sup> at 950 hPa) between 24-Oct 1800 UTC and 25-Oct 0600 UTC, in agreement with the simulated IWV in Fig. 4.a. Further east, over Dar el Beïda (Algeria, see Fig. 5.b), high specific humidity and  $\theta_e$  values are present between 500 hPa and 800 hPa on  
335 the 25-Oct 0000 UTC. The high humidity (6 g kg<sup>-1</sup>) and  $\theta_e$  (325 K) at this time come from the arrival of the moisture swept from the Atlantic. At lower levels (800 hPa to 1000 hPa), high humidity and  $\theta_e$  only happens at the station 24 h later, at 26-Oct 0000 UTC. This is because below 800 hPa, the mesoscale circulation has a strong south-to-south-easterly component (Duffourg et al., 2016; Martinet et al., 2017) which delays the arrival of the moist air masses. This can also be seen in the wind direction over Dar el Beïda on the 25-Oct 1200 UTC below 850 hPa, where a south-easterly circulation takes place. Over  
340 Mallorca, a similar vertical distribution can be observed (see Fig. 5.c.). On the 25-Oct 0000 UTC, specific humidity values as high as 6 g kg<sup>-1</sup> exist between 500 hPa and 800 hPa. Twelve hours later, the high  $\theta_e$  and specific humidity can be found in the layer 700 hPa to 800 hPa due to the delayed arrival of moisture at the low-levels. Finally, at 26-Oct 0000 UTC high  $\theta_e$  and specific humidity is located at the marine boundary layer over Mallorca.

To further understand the extent of the moisture contribution feeding convection from north Africa (NA) (Fig.1), Fig. 6 shows  
345 the mechanisms of moisture evaporation and transport. Figure 6.a shows the spatial distribution of hourly evapotranspiration simulated by CTRL-7 on the 25-Oct at 1200 UTC and the vertical updrafts of wind speed larger than 0.25 m s<sup>-1</sup>. Hourly evaporation rates of 0.3 mm h<sup>-1</sup> took place at the southern part of the NA box (North Africa) and of 0.2 mm h<sup>-1</sup> over the Algerian Atlas (northern part of the NA black box). The moisture gathers in the PBL for several days until the first convective updrafts take place over the area on the 25-Oct 1800 UTC. The radiosondes over Dar el Beïda (Fig. 5.b) show the accumulation  
350 of moisture in the lower-atmosphere (about 10 g kg<sup>-1</sup> close to 1000 hPa on the 25-Oct 1200 UTC). Vertical transport of humidity is promoted by convection during the evening of 25-Oct. At 26-Oct 0600 UTC, intense convective activity takes

place over the Mediterranean Sea, between the coast of Algeria and the island (Corsica and Sardinia). This further promotes the moisture uptake from the Sea aided by the intensified drag of low-level winds associated with convection to ensure mass-continuity (Schneider et al., 2010; Peixoto and Oort, 1992).

355 Figure 6.b represents the evapotranspiration anomaly over North Africa showing the temporal evolution of spatially averaged precipitation measured by CMORPH and simulated by CTRL-7 and of evapotranspiration as shown by GLEAM and CTRL-7. CMORPH shows spatially averaged daily precipitation over 15 mm d<sup>-1</sup> over North Africa on the 19-Oct and 20-Oct. Precipitation during these days coincided the IOP15 of HyMeX where a large band of south to north precipitation impacted regions of Africa, eastern Spain and southern France (Pantillon et al., 2015). CTRL-7 represents this precipitation but  
360 overestimates the amount. Suite to the precipitation event, daily evapotranspiration over the area reached daily spatial averages of 1.4 mm as shown by GLEAM, lasting for seven days, well above the mean evapotranspiration values during this season (0.5 mm). Albeit differences in the magnitude of evaporation, COSMO-CLM well captures this period of anomalous evapotranspiration.

Figure 6.c shows the 24h backward trajectories obtained with the HYSPLIT model, using reanalysis data from the GDAS  
365 model (see Sect. 2.1) with a resolution of 0.5°. We initialize the trajectories in a 3° x 2.5° box, at a height of 4000 m.a.s.l., over the study region CO, on the 26-Oct at 1800 UTC. The trajectories confirm the moisture transport from northern Africa, as they are located over the intense evapotranspiration area “NA” black box on the 25-Oct 1800 UTC. Two sets of trajectories are distinguishable. The first set (ellipse A in Fig. 6.c) shows the trajectories, over the Moroccan shore on the 25-Oct 1800 UTC. These trajectories travel at height between 2000 and 3000 m.a.s.l, as shown by the vertical section on the bottom of Fig.6.c.  
370 The second set (ellipse B in Fig. 6.c) shows trajectories located over northern Algeria at 25-Oct 1800 UTC. They travel at a lower height (< 1000 m) in the well mixed diurnal layer. Further trajectory analysis can be found in the supplement of this paper.

Figure 7 shows the temporal evolution of the spatially averaged moisture budget terms over the investigation areas NA and MED (see Fig. 6). The moisture budget terms have been obtained as in Lamb et al. (2012). Precipitation is considered a  
375 moisture sink, whereas evapotranspiration is a source. Moisture Flux Convergence (MFC) can be a sink or a source depending on its sign. The temporal evolution over NA (Fig. 7.a) shows that on the 25-Oct 1200 UTC the contribution of the Evaporation to IWV reaches 0.1 mmh<sup>-1</sup>, due to the wetter than usual soil over NA and the intense solar radiation. This moisture contribution is almost as large as the evaporation from the Mediterranean Sea over the MED area (0.15 mmh<sup>-1</sup>). On the 25-Oct 1800 UTC an increase in IWV takes places reaching 0.8 mmh<sup>-1</sup> over NA (Fig.1.a) due to strong Moisture Flux Convergence (MFC)  
380 associated with the Atlantic moisture brought by the south-westerly flow. Over MED (Fig 7.b) we can see a stable Evaporation during the period as well as an enhanced MCF, especially after 25-Oct 1800 UTC. These two contributions build up overseas until the 26-Oct 0600 UTC when convection triggers.

## 4 Nudging Effects on Convection

### 4.1 Precipitation

385 The COSMO-CLM simulations were able to represent the event over the island on both the 7 km and the 2.8 km configurations at the right time. CTRL-7 performed well in representing the location of maximum precipitation over the windward slope of the Corsican mountains (see Fig. 8.a and Fig. 3.b). CTRL-2.8 showed a worse representation of the location of the maximum as it shifted it towards the crests of the mountain mainly and also to the lee side (see Fig. 8.c), but represented better the amount than CTRL-7. CTRL-2.8 represented more isolated precipitation structures, located over the mountain crests. Representing  
390 more localized structures is a well identified effect of reaching convection permitting resolutions (Chan et al., 2012; Fosser et al., 2016)

The GPS-ZTD nudging induced for both model resolutions a decrease in the accumulated totals. In the case of NDG-7 this occurred over the windward side of the mountain, improving the agreement with the observations (Fig. 3.b). NDG-2.8 showed the same location of the maxima as CTRL-2.8 with a too large reduction with values below 20 mm.

395 To validate quantitatively our simulations against rain gauges, Table 2 shows the Root Mean Square Error (RMSE), the hourly standard deviation difference ( $OBS_{\sigma} - MOD_{\sigma}$ ), the spatially averaged differences ( $\overline{OBS} - \overline{MOD}$ ), the accumulated precipitation standard deviation difference ( $OBS_{\sigma} - MOD_{\sigma}$ ) and the difference of maximum precipitation ( $OBS_{max} - MOD_{max}$ ). A description of the metrics can be found in the Annex. The results show the overestimation of maximum and spatially average precipitation by CTRL-7 in excess of 185 mm and 10.4 mm, respectively, as well as of the standard deviations  
400 (-32 mm). The RMSE for hourly precipitation was of 3.1 mm. The reduction caused by the GPS-ZTD nudging was beneficial for the representation of maximum accumulated precipitation in NDG-7, now in excess of 58 mm compared to the observations, of the accumulated precipitation standard deviation (-0.7 mm) and of the RMSE (2.6 mm). CTRL-2.8 showed a good performance with better values than CTRL-7 for maximum (excess of 3 mm) and spatially averaged accumulated precipitation (14.6 mm) as well as of the standard deviation differences with, however, the same RMSE (3.1 mm). The GPS-  
405 ZTD dried excessively the NDG-2.8 simulations bringing worse scores. Only the RMSE was improved (2.7 mm), similarly to NDG-7, possibly due to a better representation of the location of precipitation relevant for the interpolation of the COSMO-CLM simulations to the rain gauges location.

### 4.2 Atmospheric Moisture

As introduced in Section 3, we assess the accuracy of model moisture outputs and the impact of nudging GPS-ZTD, comparing  
410 independent humidity measurements from radiosondes. The reference run, CTRL-2.8, has MAE values of 2.7 mm, with MB of 0.38 mm and AI of 0.89. These values are similar to those of CTRL-7 albeit a slight improvement of the MB and the AI. Nudging GPS-ZTD data, improves further the scores bringing the MAE of IWV to 2 mm for NDG-7 and NDG-2.8 and the MB to -0.04 mm and -0.08 mm, respectively. In this sense, both the 7 km and the 2.8 km simulations endure an improvement.

Figure 9.a shows the spatially averaged temporal evolution of IWV over the study region CO. The hours prior to precipitation initiation (26-Oct 1300 UTC) were characterized by an IWV pick up starting at 26-Oct 0000 UTC. All simulations showed this, albeit the IWV amount over CO for NDG-7 and NDG-2.8 was 5 mm higher than for CTRL-7 and CTRL-2.8. This was due to represented precipitation over the island until the night of 24-Oct in the NDG runs, hence inducing a much wetter boundary layer (not shown). By 26-Oct 1000 UTC, an intense moisture increase takes place over the island. As described in Sect. 3.3, this is the time when the Atlantic, Mediterranean and African moisture reached CO. At this time, all simulations show the same mean IWV (27 mm) which lasts for 4 hours. Given no GPS stations are located over Africa or the Mediterranean Sea, the south-westerly moisture is only weakly impacted by the GPS-ZTD nudging during these first four hours of the event over CO. At 26-Oct 1400 UTC, the CTRL and NDG runs start to diverge and between 26-Oct 1600 UTC and 27-Oct 0600 UTC, NDG-7 and NDG-2.8 show ca. 4 mm less than their CTRL counterparts do. This is due to the impact of the GPS measurements over the island.

To understand at which levels the humidity reduction was most effective Figure 9.b shows box and whiskers plots between 500 hPa and the surface. At 500 hPa, a specific humidity reduction of  $0.2 \text{ g kg}^{-1}$  took place for median values in the 7 km simulation (-13 %). The decrease was weaker in the 2.8 km grid with a reduction of  $0.05 \text{ g kg}^{-1}$  (-3 %). At 700 hPa the specific humidity decrease was about  $0.4 \text{ g kg}^{-1}$  for median values (-8 %) for both resolutions. At 950 hPa, the humidity reduction was larger in the 7 km (-8 %) than in the 2.8 km run (-2%). Finally, at 2 m height the reduction was of -7 % for 7 km and of -3 % for 2.8 km

Figure 10 represents the MAE and the MB of specific humidity profiles between 500 hPa and 950 hPa for the same set of radiosondes. The period of validation is 26-Oct 0000 UTC to 28-Oct 0000 UTC and the area is larger than that of Corsica. This is done to assess the overall performance of the model with as many radiosondes as possible (Fig. 1). Between 600 hPa and 950 hPa, the MAE of specific humidity of CTRL-7 and CTRL-2.8 is between  $0.7 \text{ g kg}^{-1}$  (600 hPa) and  $1.3 \text{ g kg}^{-1}$  (925 hPa). The MB of the profile shows that this error comes from an underestimation of specific humidity by COSMO-CLM below 650 hPa, which is largest below 900 hPa. Over 650 hPa, the simulations overestimated the specific humidity. The GPS-ZTD nudging improves the MAE of the humidity profile between 650 hPa and 925 hPa for both resolutions. The MAE of NDG-7 is now within the range  $0.6 \text{ g kg}^{-1}$  (600 hPa) and  $1.1 \text{ g kg}^{-1}$  (925 hPa) and the improvement reaches the 950 hPa level. For NDG-2.8, the MAE is between  $0.8 \text{ g kg}^{-1}$  (650 hPa) and  $1.2 \text{ g kg}^{-1}$  (900 hPa) but an improvement is only achieved down to 925 hPa. The MB is closer to zero at the same atmospheric layers (650 hPa to 900 hPa) for both resolutions albeit showing better results for the 7 km simulation. The correction for LFT moisture is larger in the 7 km runs than in the 2.8 km, probably due to the larger number of observations included in the nudging in this simulation because of larger simulation domains (see Fig. 1). These values of the MAE and Mean Bias are of the same order as the validation of the RMSE of specific humidity profiles between reanalyses data and Lidar measurements from Duffourg et al. (2016).

Below 900 hPa, the GPS-ZTD nudging was not able to correct sufficiently the dry bias of the model. Both CTRL runs show difficulties in representing the steeper gradient shown by the radiosondes and the correction induced by the GPS-ZTD nudging is not enough to moist sufficiently the PBL during this event. Overall, COSMO-CLM shows a good performance in

representing the integrated atmospheric moisture fields and humidity over 900 hPa at both model resolutions. The 2.8 km simulation was initially more accurate, but the nudging brings both to similar accuracy values.

#### 450 **4.3 Instability reduction and increase of free-tropospheric mixing**

The two affected processes, which exerted the largest control on precipitation reduction, were atmospheric latent instability reduction and dry air entrainment, both investigated in this section. The changes in these two processes start to play a role immediately after the first hour of large IWV differences i.e. after 26-Oct 1600 UTC this is so for both the 7 km and the 2.8 km simulations.

455 Figure 11 shows the vertical cross-sections of Equivalent Potential Temperature ( $\theta_e$ ), specific humidity and the wind along the direction of the mean horizontal wind (purple transect in Fig. 1) over the island at 26-Oct 1700 UTC. CTRL-7 and CTRL-2.8 show  $\theta_e$  values over 322 K from the surface up to 500 hPa showing the upward transport of moist low-level air masses. After applying the GPS-ZTD nudging, NDG-7 shows reduced values of  $\theta_e$  (310 K) close to the ground (see 2 m specific humidity in Fig.9.b) over the island and at 700 hPa (312 K) showing a less favourable environment for convection  
460 development. The 2.8 km simulation, for its part, showed a weak reduction of  $\theta_e$  at the windward side of the mountain (316 K) as a result of the GPS-ZTD nudging compared to the NDG-7. However, at the lee side between 600 hPa and 900 hPa,  $\theta_e$  is reduced in NDG-2.8 by -8 K (compared to CTRL-2.8, 318 K), this is shown in Fig. 11.c and Fig. 11.d. The consequence for the updrafts was a change in their timing location and intensity with less penetrating updrafts (see Fig. 11.d).

Figure 12 shows that median CAPE is reduced as a result of the GPS-ZTD nudging for both resolutions from 310 J kg<sup>-1</sup> in  
465 CTRL-7 to 190 J kg<sup>-1</sup> in NDG-7 (-39 %) and from 600 J kg<sup>-1</sup> in CTRL-2.8 to 410 J kg<sup>-1</sup> in NDG-2.8 (-32 %). Since COSMO-CLM selects the lowest 50 hPa as the mean layer to compute CAPE (mixed layer), a decrease of humidity close to ground implies a relevant impact on atmospheric instability conditions. COSMO-CLM in the 2.8 km resolution represented larger latent instability than 7 km for this event. Median KO-index increased from -2.7 K, in CTRL-7 to -1.5 K in NDG-7 (+ 44 %) where lower KO-index indicates more potential for storm development under favourable large-scale conditions. The narrower  
470 simulation domains of the 2.8 km simulations (see Sect. 2.2.2) render the impact of the GPS-ZTD nudging on KO-index weaker given the inability to represent changes on the large-scale pressure distribution. The overall decrease in the median moisture flux implies a drier ground level and a drier LFT. This means that the air entrained in the convective updrafts is drier than that of the reference runs (CTRL). The median moisture flux is reduced by about 13 % in NDG-7 and about 5% in CTRL-2.8 at 700 hPa. At the PBL, the moisture flux is also reduced. The changes in moisture flux between CTRL-7 and NDG-7 are  
475 larger than their 2.8 km counterparts. This is due to two factors, first, the changes in specific humidity are slightly weaker in the 2.8 km runs as compared to 7 km and second, the horizontal wind speed and direction in the 7 km runs are modified as a result of the GPS-ZTD nudging. For instance, at 950 hPa, extreme horizontal wind speeds are reduced by -8 % from CTRL-7 to NDG-7. This impact is not observed in the 2.8 km runs.

Overall, the humidity reduction caused by the GPS-ZTD nudging, locally over Corsica, reduced the amount of instability (as shown by CAPE and KO-index) as well as humidity at the LFT (demonstrated by the changes in specific humidity and moisture flux).

#### 4.4 Impact on the low-pressure system and mesoscale winds

Besides impacting the representation of the local conditions of humidity, instability and buoyancy, the GPS-ZTD nudging affected the representation of the low-pressure system.

In the early morning of 26-Oct-2016, the centre of the upper-level low was located over the north-western part of the Iberian Plateau. The GPS-ZTD nudging induced moisture reductions of 7 mm in IWV at that location in the NDG-7 simulations, with very large reductions in the range 1-2 g kg<sup>-1</sup> from the ground up to 700 hPa (not shown). The progression of the pressure-low toward southern France was effective in twelve hours and at 1500 UTC, the PMSL was of 995hPa at the Rhône Valley (CTRL-7). The centre of the Low extended toward the Alps at 2300 UTC. Drying of the atmospheric column, due to the GPS-ZTD nudging, also took place at this region between the 25-Oct and the 28-Oct (not shown). At 2300 UTC on the 20-Oct, over the Cévennes-Vivarais area, differences in IWV were of 3 mm between CTRL-7 and NDG-7. Figure 13 shows the differences in PMSL on the 26-Oct 2300 UTC between NDG-7 and CTRL-7 as well as the wind fields at 950 hPa. The GPS-ZTD nudging increased by 10 hPa the PMSL at the centre of the system and up to 2 hPa between Brittany (France) and the Balearic Islands (Spain). The drying over France and the Iberian Peninsula induced a weaker low-pressure system in NDG-7, this changed the cyclonic wind circulation from a south-westerly to west-south-westerly flow and a reduction of the horizontal wind speeds. The largest impact was observed at the 950 hPa level albeit relevant differences affecting Corsica exist between 850 hPa and 1000 hPa. The reduction of the horizontal wind speeds is demonstrated through box-whisker plots in Fig. 12. This difference in horizontal wind speed does not exist in the 2.8 km runs. This hampered orographic lifting at the mountain foothills and ahead of the island reducing triggering of new cells and weakening the convective updrafts.

#### 500 4.5 10-min vs. 1-hour nudging

To discern the added value of nudging GPS-ZTD with a 10-minute frequency with respect to lower nudging frequencies, we carried out additional simulations with COSMO-CLM with a 1 h frequency initialized on the 20-Oct-2012 0000 UTC. These simulations have the same model settings as the original simulations (Section 2.2.2) except for the changes in nudging frequency (named with the suffix 1h). The initialization time is also different to avoid the computational cost of running the whole autumn season but is early enough to mind the Atlantic and African moisture transports described in Section 3.3. They show analogue features to those presented in Section 2.2.2 and hence are used for validation of the 1 h frequency nudging impacts

Table 3 shows a validation of the additional runs against rain gauges, as in Table 2. Nudging GPS-ZTD data with a 1h frequency brings a slightly larger reduction of the precipitation maximum and the hourly standard deviation for NDG-7-1h as compared to the 10-minute frequency (NDG-7). The RMSE, the standard deviation and the mean of accumulated precipitation showed



no relevant differences between NDG-7 and NDG-7-1h. This aspect is even clearer in the case of 2.8 km. No perceptible differences exist for the validation metrics between NDG-2.8-1h and NDG-2.8. Similarly to the validation metrics, the spatial distribution shows no relevant differences between the 1 h and the 10 min frequency nudging. The spatial distributions are shown in Fig. S.4 of the supplementary material.

## 515 5 Conclusions

The pathways of moisture and its interaction with convection are not fully understood (Stevens, 2005; Sherwood et al., 2010; Ahrens and Samson, 2010). A deeper understanding of moist processes is relevant to improve the representation of heavy precipitation by numerical atmospheric models in order to support the mitigation and prevention of its hazards. This study aimed at assessing the sensitivity of convective precipitation and underlying mechanisms to variations of the atmospheric  
520 moisture distribution. With this purpose, we presented an in-depth analysis of HyMeX IOP16 with special focus on the complex orographic region of Corsica. We showed novel insights on the role of remote moisture transports for this event and the sensitivity of precipitation representation to high frequency GPS-ZTD nudging. The main findings of this diagnostic study are summarized in the following:

- Large atmospheric moisture amounts (IWV~ 40 mm) precondition the areas of convective activity, namely, southern  
525 France, the Gulf of Lions, Corsica, Sardinia, the middle Mediterranean and northeastern Italy, in agreement with previous investigations in the region (Khodayar et al., 2016). These very wet air masses reach southern France and the Gulf of Lions about 12 h prior to precipitation initiation and the central Mediterranean about 4 h prior to initiation. A low-level convergence line located between France and the Balearic Islands (Duffourg et al., 2016; Martinet et al., 2017) delays the arrival of low-level moisture at Corsica and the Italian Peninsula.
- The transport of moisture feeding the convective cells arises from the action of the upper-level pressure low through  
530 two mechanisms. Firstly, the associated front, sweeps atmospheric moisture from the Atlantic to the Mediterranean in the course of 36 hours. Secondly, evaporated moisture over the Mediterranean and north Africa between 25-Oct 1800 UTC and 26-Oct 1200 UTC is transported by the south-westerly flow towards Corsica, feeding of the convective systems.
- Northern Africa has been identified as a source of moisture for this event, caused by intense evapotranspiration  
535 between 21-Oct and 28-Oct due to intense solar radiation and precipitation impacting the region two days earlier. After 25-Oct, the intense south-westerly flow and the convective activity brought the moisture up north in the course of 24 h to 30 h as shown by backward trajectories and model output.

COSMO-CLM was able to represent this event over Corsica with a good agreement on the timing for both resolutions but an  
540 overestimation of precipitation in CTRL-7, well corrected by the GSP-ZTD nudging. Overall, the representation of humidity during the event was good and the GPS-ZTD nudging helped to further reduce the model humidity biases. In this regard

- 545
- The precipitation overestimation in the 7 km run was well corrected by the GPS-ZTD nudging. Regarding the 2.8 km simulations, CTRL-2.8 performed well in representing the maximum and the spatial averages but the GPS-ZTD nudging reduced excessively the total precipitation. The impact of nudging GPS-ZTD with a 1 h frequency or a the 10-minute frequency showed no relevant differences.
  - The reference runs (CTRL-7 and CTRL-2.8) performed overall well in reproducing the moisture distribution during the event. The GPS-ZTD nudging improved the representation of IWV reducing the MAE of IWV. Regarding the vertical distribution of humidity, the GPS-ZTD nudging improved by 25 % the MAE below 650 hPa in the 7 km simulation and by 8% between 650 hPa and 925 hPa in the 2.8 km resolution. The weaker improvement at the PBL is because the model is unable to represent the abrupt humidity gradient of the lowest layers. Even if the GPS-ZTD correction is beneficial, it is not sufficient to overcome the humidity biases at this level.
- 550

The impact of the GPS-ZTD nudging during the case study has been assessed with the following conclusions:

- Heavy precipitation showed a large sensitivity to the moisture variations, implying a strong reduction of the maximum totals (-49 % for 7 km and -16 % for 2.8 km) arising from less intense convection and a lower number of triggered cells.
  - The two affected processes which exerted the largest control for precipitation reduction were the reduction of atmospheric instability over the island (-35 % CAPE) and the drying of the LFT bringing more dry air entrainment into the convective updrafts (-13 % moisture flux at 700 hPa for 7 km and -5 % for 2.8 km).
  - Additionally, the 7 km simulations showed an impact on the large-scale surface pressure and the associated circulation given the larger simulation domains. The GPS-ZTD nudging dried the atmospheric levels over Iberia and France, weakening the Low-Pressure system. This induced in turn a decrease in horizontal wind speed and a veering of the direction toward a west-south-westerly.
- 555
- 560

The unique opportunity provided by the synergy of high-resolution atmospheric modelling, very frequent data nudging and high-resolution humidity datasets enables the study of moisture and convection interactions in a selected case study of heavy precipitation. We showed the benefit of nudging GPS-ZTD for the simulation of the vertical profile and integrated amount of atmospheric humidity and for precipitation in a convection parameterized set-up (7 km). This is relevant since coarse resolution simulations will still be needed as providers of forcing data and therefore GPS-ZTD nudging can reduce moisture uncertainties at these grid lengths. The performance of CTRL-2.8 was acceptable without the GPS-ZTD nudging. This highlights the added value of convection permitting resolutions for this case able to provide a fair precipitation forecast even in the presence of the addressed humidity biases. Also noteworthy is the large sensitivity to variations of the LFT moisture showed by the model. Recent observational studies have highlighted the linkage between intense convective precipitation and a humid LFT (Schiro and Neelin, 2019; Virman et al., 2018), hence the relevance of the ability to represent such sensitivity. This study also points out one of the GPS-ZTD nudging drawbacks. Being an integrated quantity, GPS-ZTD nudging struggles to correct the vertical distribution of humidity, in this case particularly in the lower-troposphere. Lastly, this study focuses on a single case study; therefore, the results presented here should be extended to other events of the region to allow for generalization. In a further

565

570

575

publication, the authors evaluate the impact of GPS-ZTD nudging on the SOP1 period of the HyMeX campaign considering the sensitivity of all IOPs in this autumn season.

## **6. Code Availability**

580 The COSMO-CLM model is only accessible to members of the Climate Limited-area Modelling Community and access is granted upon request. Parts of the model documentation are freely available at <http://www.cosmo-model.org/content/model/documentation/core/default.htm>

## **7. Data Availability**

Two further publications using these nudging simulations are on-going. Therefore, these are not yet available for the open public. However, the data used to produce the figures showing results on the nudging simulations (Figures 2, 4, 6.a, 6.b, 8, 9, 585 10, 11, 12, 13; and Tables 1, 2 and 3) are accessible in at <https://doi.org/10.5445/IR/1000097457>. The observational data used in the figures within this manuscript are obtained from the referenced data sets and their access depends on the restrictions of the producing institutions.

## **8. Author Contributions**

590 SK designed and planned the experiments. ACA carried out as part of his PhD the nudging experiments under the supervision of SK. ACA and SK analysed the results and wrote the manuscript.

## **9. Competing Interests**

The authors declare that they have no conflict of interest.

## **10. Acknowledgements**

595 We acknowledge Oliver Bock and the Laboratoire de Recherche En Géodésie (LAREG) of the French Institute of the Geographic and Forest Information (IGN) for their providing of the GPS-ZTD data set. We also acknowledge Météo-France and the HyMeX program for supplying the Rain gauges and radiosonde data supported by grants MISTRALS/HyMeX and ANR-11-BS56-0005 IODA-MED. We would like to thank the German Weather Service (DWD) and the CLM-Community for their providing of the COSMO-CLM model, and especially Ulrich Schättler and Christoph Schraff for their support in carrying out the nudging experiments. We are also thankful to the European Centre for Medium-Range Weather Forecasts 600 (ECMWF) for their Integrated Forecasting System (IFS) analyses. We thank as well the teams of HYSPLIT at the NOAA Air

Resources Laboratory, CMORPH at the Climate Prediction Center (CPC) and GLEAM for their data sets. We thank the reviewers for their fruitful comments. Finally, we would like to thank the hosting institution, the Karlsruhe Institute of Technology (KIT).

## 11. Financial support

605 This research work has been supported by the Bundesministerium für Bildung und Forschung (BMBF; German Federal Ministry of Education and Research) project PREMIUM 01LN1319A.

## 12. References

- Adler, B., Kalthoff, N., Kohler, M., Handwerker, J., Wieser, A., Corsmeier, U., Kottmeier, C., Lambert, D., and Bock, O.: The variability of water vapour and pre-convective conditions over the mountainous island of Corsica, *Quarterly Journal of the Royal Meteorological Society*, 142, 335–346, <https://doi.org/10.1002/qj.2545>, 2015.
- 610 Ahrens, C. D. and Samson, P. J.: *Extreme Weather and Climate*, Cengage Learning, 2010.
- Andersson, T., Andersson, M., Jacobsson, C., and Nilsson, S.: Thermodynamic indices for forecasting thunderstorms in southern Sweden, *Meteorological Magazine*, 118, 1989.
- Bevis, M., Businger, S., Chiswell, S., Herring, T. A., Anthes, R. A., Rocken, C., and Ware, R. H.: GPS Meteorology: Mapping Zenith Wet Delays onto Precipitable Water, *Journal of Applied Meteorology*, 33, 379–386, [https://doi.org/10.1175/1520-0450\(1994\)033<0379:gmmzwd>2.0.co;2](https://doi.org/10.1175/1520-0450(1994)033<0379:gmmzwd>2.0.co;2), 1994.
- 615 Bitew, M. M. and Gebremichael, M.: Evaluation of satellite rainfall products through hydrologic simulation in a fully distributed hydrologic model, *Water Resour. Res.*, 47, 45, <https://doi.org/10.1029/2010WR009917>, 2011.
- Bock, O., Bossler, P., Pacione, R., Nuret, M., Fourrié, N., and Parracho, A.: A high-quality reprocessed ground-based GPS dataset for atmospheric process studies, radiosonde and model evaluation, and reanalysis of HyMeX Special Observing Period, *Quarterly Journal of the Royal Meteorological Society*, 142, 56–71, <https://doi.org/10.1002/qj.2701>, 2016.
- Businger, S., Chiswell, S. R., Bevis, M., Duan, J., Anthes, R. A., Rocken, C., Ware, R. H., Exner, M., VanHove, T., and Solheim, F. S.: The Promise of GPS in Atmospheric Monitoring, *Bulletin of the American Meteorological Society*, 77, 5–18, [https://doi.org/10.1175/1520-0477\(1996\)077<0005:tpogia>2.0.co;2](https://doi.org/10.1175/1520-0477(1996)077<0005:tpogia>2.0.co;2), 1996.
- 625 Caldas-Alvarez. A.: *Atmospheric Moisture Effects on Deep Convection in the Western Mediterranean*, KIT Scientific Publishing, VI, 237, <http://dx.doi.org/10.5445/KSP/1000097100>, 2019.
- Chan, S. C., Kendon, E. J., Fowler, H. J., Blenkinsop, S., Ferro, C. A. T., and Stephenson, D. B.: Does increasing the spatial resolution of a regional climate model improve the simulated daily precipitation?, *Climate Dynamics*, 41, 1475–1495, <https://doi.org/10.1007/s00382-012-1568-9>, 2012.

- 630 Chazette, P., Flamant, C., Shang, X., Totems, J., Raut, J.-C., Doerenbecher, A., Ducrocq, V., Fourrié, N., Bock, O., and Cloché, S.: A multi-instrument and multi-model assessment of atmospheric moisture variability over the western Mediterranean during HyMeX, *Quarterly Journal of the Royal Meteorological Society*, 142, 7–22, <https://doi.org/10.1002/qj.2671>, 2015.
- Chazette, P., Flamant, C., Raut, J.-C., Totems, J., and Shang, X.: Tropical moisture enriched storm tracks over the Mediterranean and their link with intense rainfall in the Cevennes-Vivarais area during HyMeX, *Quarterly Journal of the*
- 635 *Royal Meteorological Society*, 142, 320–334, <https://doi.org/10.1002/qj.2674>, 2015b.
- Cress, A., Anlauf, H., Bitzer, H. W., Rhodin, A., Schraff, C., Helmert, K., and Stephan, K. (Eds.): *Global and regional impact studies at the German Weather Service (DWD)*, Sedona (USA), 2012.
- Di Girolamo, P., Flamant, C., Cacciani, M., Richard, E., Ducrocq, V., Summa, D., Stelitano, D., Fourrié, N., and Saïd, F.: Observation of low-level wind reversals in the Gulf of Lion area and their impact on the water vapour variability, *Q.J.R. Meteorol. Soc.*, 142, 153–172, <https://doi.org/10.1002/qj.2767>, 2016.
- 640 Doms, G., Förstner, J., Heise, E., Herzog, H. -J., Mironov, D., Raschendorfer, M., Reinhardt, T., Ritter, B., Schrodin, R., Schulz, J. -P., and Vogel, G.: *A Description of the Nonhydrostatic Regional COSMO Model Part II: Physical Parameterization*, P.O. Box 100465, 63004, Offenbach, Germany, 2011.
- Duan, J., Bevis, M., Fang, P., Bock, Y., Chiswell, S., Businger, S., Rocken, C., Solheim, F., van Hove, T., Ware, R., McClusky, S., Herring, T. A., and King, R. W.: GPS Meteorology: Direct Estimation of the Absolute Value of Precipitable Water, *Journal of Applied Meteorology*, 35, 830–838, [https://doi.org/10.1175/1520-0450\(1996\)035<0830:gmdeot>2.0.co;2](https://doi.org/10.1175/1520-0450(1996)035<0830:gmdeot>2.0.co;2), 1996.
- 645 Ducrocq, V., Braud, I., Davolio, S., Ferretti, R., Flamant, C., Jansa, A., Kalthoff, N., Richard, E., Taupier-Letage, I., Ayrál, P.-A., Belamari, S., Berne, A., Borga, M., Boudevillain, B., Bock, O., Boichard, J.-L., Bouin, M.-N., Bousquet, O., Bouvier, C., Chiggiato, J., Cimini, D., Corsmeier, U., Coppola, L., Cocquerez, P., Defer, E., Delanoë, J., Di Girolamo, P., Doerenbecher, A., Drobinski, P., Dufournet, Y., Fourrié, N., Gourley, J. J., Labatut, L., Lambert, D., Le Coz, J., Marzano, F. S., Molinié, G., Montani, A., Nord, G., Nuret, M., Ramage, K., Rison, W., Roussot, O., Saïd, F., Schwarzenboeck, A., Testor, P., van Baelen, J., Vincendon, B., Aran, M., and Tamayo, J.: HyMeX-SOP1: The Field Campaign Dedicated to Heavy Precipitation and Flash Flooding in the Northwestern Mediterranean, *Bulletin of the American Meteorological*
- 655 *Society*, 95, 1083–1100, <https://doi.org/10.1175/bams-d-12-00244.1>, 2014.
- Ducrocq, V., Davolio, S., Ferretti, R., Flamant, C., Santaner, V. H., Kalthoff, N., Richard, E., and Wernli, H.: Introduction to the HyMeX Special Issue on ‘Advances in understanding and forecasting of heavy precipitation in the Mediterranean through the HyMeX SOP1 field campaign’, *Quarterly Journal of the Royal Meteorological Society*, 142, 1–6, <https://doi.org/10.1002/qj.2856>, 2016.
- 660 Duffourg, F. and Ducrocq, V.: Origin of the moisture feeding the Heavy Precipitating Systems over Southeastern France, *Natural Hazards and Earth System Science*, 11, 1163–1178, <https://doi.org/10.5194/nhess-11-1163-2011>, 2011.

- Duffourg, F., Nuissier, O., Ducrocq, V., Flamant, C., Chazette, P., Delanoë, J., Doerenbecher, A., Fourrié, N., Di Girolamo, P., Lac, C., Legain, D., Martinet, M., Saïd, F., and Bock, O.: Offshore deep convection initiation and maintenance during the HyMeX IOP 16a heavy precipitation event, *Quarterly Journal of the Royal Meteorological Society*, 142, 259–274, <https://doi.org/10.1002/qj.2725>, 2016.
- 665
- Fosser, G., Khodayar, S., and Berg, P.: Climate change in the next 30 years: What can a convection-permitting model tell us that we did not already know?, *Climate Dynamics*, 48, 1987–2003, <https://doi.org/10.1007/s00382-016-3186-4>, 2016.
- Funatsu, B. M., Rysman, J.-F., Claud, C., and Chaboureaud, J.-P.: Deep convective clouds distribution over the Mediterranean region from AMSU-B/MHS observations, *Atmospheric Research*, 207, 122–135, <https://doi.org/10.1016/j.atmosres.2018.03.003>, 2018.
- 670
- Gilabert, J. and Llasat, M. 4C.: Circulation weather types associated with extreme flood events in Northwestern Mediterranean, *International Journal of Climatology*, 38, 1864–1876, <https://doi.org/10.1002/joc.5301>, 2017.
- González-Zamora, Á., Sánchez, N., Martánez, J., Gumuzzio, Á., Piles, M.ggg, and Olmedo, E.: Long-term SMOS soil moisture products: A comprehensive evaluation across scales and methods in the Duero Basin (Spain), *Physics and Chemistry of the Earth, Parts A/B/C*, 83-84, 123–136, <https://doi.org/10.1016/j.pce.2015.05.009>, 2015.
- 675
- Guerova, G., Jones, J., Douša, J., Dick, G., Haan, S. d., Pottiaux, E., Bock, O., Pacione, R., Elgered, G., Vedel, H., and Bender, M.: Review of the state of the art and future prospects of the ground-based GNSS meteorology in Europe, *Atmospheric Measurement Techniques*, 9, 5385–5406, <https://doi.org/10.5194/amt-9-5385-2016>, 2016.
- Habib, E., Haile, A. T., Tian, Y., and Joyce, R. J.: Evaluation of the High-Resolution CMORPH Satellite Rainfall Product Using Dense Rain Gauge Observations and Radar-Based Estimates, *J. Hydrometeor.*, 13, 1784–1798, <https://doi.org/10.1175/JHM-D-12-017.1>, 2012.
- 680
- Honda, T. and Kawano, T.: How does mid-tropospheric dry air affect the evolution of supercellular convection?, *Atmospheric Research*, 157, 1–16, <https://doi.org/10.1016/j.atmosres.2015.01.015>, 2015.
- Jansa, A., Genoves, A., Picornell, M. A., Campins, J., Riosalido, R., and Carretero, O.: Western Mediterranean cyclones and heavy rain. Part 2: Statistical approach, *Meteorological Applications*, 8, 43–56, <https://doi.org/10.1017/s1350482701001049>, 2001.
- 685
- Joyce, R. J., Janowiak, J. E., Arkin, P. A., and Xie, P.: CMORPH: A Method that Produces Global Precipitation Estimates from Passive Microwave and Infrared Data at High Spatial and Temporal Resolution, *Journal of Hydrometeorology*, 5, 487–503, [https://doi.org/10.1175/1525-7541\(2004\)005<0487:camtpg>2.0.co;2](https://doi.org/10.1175/1525-7541(2004)005<0487:camtpg>2.0.co;2), 2004.
- 690
- Keil, C., Röpnack, A., Craig, G. C., and Schumann, U.: Sensitivity of quantitative precipitation forecast to height dependent changes in humidity, *Geophysical Research Letters*, 35, <https://doi.org/10.1029/2008gl033657>, 2008.
- Khodayar, S., Fosser, G., Berthou, S., Davolio, S., Drobinski, P., Ducrocq, V., Ferretti, R., Nuret, M., Pichelli, E., Richard, E., and Bock, O.: A seamless weather-climate multi-model intercomparison on the representation of a high impact weather

- 695 event in the western Mediterranean: HyMeX IOP12, *Q.J.R. Meteorol. Soc.*, 142, 433–452, <https://doi.org/10.1002/qj.2700>, 2016.
- Khodayar, S., Kalthoff, N., and Kottmeier, C.: Atmospheric conditions associated with heavy precipitation events in comparison to seasonal means in the western mediterranean region, *Climate Dynamics*, 51, 951–967, <https://doi.org/10.1007/s00382-016-3058-y>, 2016.
- 700 Krichak, S. O., Barkan, J., Breitgand, J. S., Gualdi, S., and Feldstein, S. B.: The role of the export of tropical moisture into midlatitudes for extreme precipitation events in the Mediterranean region, *Theoretical and Applied Climatology*, 121, 499–515, <https://doi.org/10.1007/s00704-014-1244-6>, 2014.
- Lamb, P. J. and Ports, D. H.: Investigation of Large-Scale Atmospheric Moisture Budget and Land Surface Interactions over U. S. Southern Great Plains including for CLASIC (June 2007), *Journal of Hydro Meteorology*, <https://doi.org/10.1175/JHM-D-12-01.1>, 2012.
- 705 Lee, K.-O., Flamant, C., Duffourg, F., Ducrocq, V., and Chaboureau, J.-P.: Impact of upstream moisture structure on a back-building convective precipitation system in south-eastern France during HyMeX IOP13, *Atmospheric Chemistry and Physics*, 18, 16845–16862, <https://doi.org/10.5194/acp-18-16845-2018>, 2018.
- Leuenberger, D., Stoll, M., and Roches, A.: Description of some convective indices implemented in the COSMO model, Deutscher Wetterdienst (DWD), [http://www.cosmo-](http://www.cosmo-model.org/content/model/documentation/techReports/docs/techReport17.pdf)  
710 [model.org/content/model/documentation/techReports/docs/techReport17.pdf](http://www.cosmo-model.org/content/model/documentation/techReports/docs/techReport17.pdf), last access: 22 July 2019, 2010.
- Llasat, M. C., Llasat-Botija, M., Prat, M. A., Porcú, F., Price, C., Mugnai, A., Lagouvardos, K., Kotroni, V., Katsanos, D., Michaelides, S., Yair, Y., Savvidou, K., and Nicolaidis, K.: High-impact floods and flash floods in Mediterranean countries: The FLASH preliminary database, *Advances in Geosciences*, 23, 47–55, [https://doi.org/10.5194/adgeo-23-47-](https://doi.org/10.5194/adgeo-23-47-2010)  
715 [2010](https://doi.org/10.5194/adgeo-23-47-2010), 2010.
- Maranan, M., Fink, A. H., Knippertz, P., Francis, S. D., Akpo, A. B., Jegede, G., and Yorke, C.: Interactions between Convection and a Moist Vortex Associated with an Extreme Rainfall Event over Southern West Africa, *Mon. Wea. Rev.*, 147, 2309–2328, <https://doi.org/10.1175/MWR-D-18-0396.1>, 2019.
- Martens, B., Miralles, D. G., Lievens, H., van der Schalie, R., Jeu, R. A. M. d., Fernández-Prieto, D., Beck, H. E., Dorigo, W. A., and Verhoest, N. E. C.: GLEAM v3: Satellite-based land evaporation and root-zone soil moisture, *Geoscientific Model Development*, 10, 1903–1925, <https://doi.org/10.5194/gmd-10-1903-2017>, 2017.
- 720 Martinet, M., Nuissier, O., Duffourg, F., Ducrocq, V., and Ricard, D.: Fine-scale numerical analysis of the sensitivity of the HyMeX IOP16a heavy precipitating event to the turbulent mixing-length parametrization, *Quarterly Journal of the Royal Meteorological Society*, 143, 3122–3135, <https://doi.org/10.1002/qj.3167>, 2017.

- 725 Miralles, D. G., Holmes, T. R. H., Jeu, R. A. M. de, Gash, J. H., Meesters, A. G. C. A., and Dolman, A. J.: Global land-surface evaporation estimated from satellite-based observations, *Hydrol. Earth Syst. Sci.*, 15, 453–469, <https://doi.org/10.5194/hess-15-453-2011>, 2011.
- Nuret, M.: HyMeX domain precipitation amount, SEDOO OMP. Doi: 10.6096/mistrals-hymex. 904, 2013.
- Pantillon, F., Chaboureaud, J. P. and Richard, E.: Remote impact of North Atlantic hurricanes on the Mediterranean during episodes of intense rainfall in autumn 2012, *Q. J. R. Meteorol. Soc.*, 141, 967-978, <https://doi.org/10.1002/qj.2419>, 2015.
- 730 Peixoto, J. P. and Oort, A. H.: *Physics of Climate*. American Inst. Of Physics, 1992.
- Pinto, J. G., Ulbrich, S., Parodi, A., Rudari, R., Boni, G., and Ulbrich, U.: Identification and ranking of extraordinary rainfall events over Northwest Italy: The role of Atlantic moisture, *Journal of Geophysical Research: Atmospheres*, 118, 2085–2097, <https://doi.org/10.1002/jgrd.50179>, 2013.
- Röhner, L., Nerding, K. U. and Corsmeier, U.: Diagnostic Study of a Heavy Precipitation Event over Spain by investigation of moisture trajectories. *Q. J. R. Meteorol. Soc.*, 142, 287-297, <https://doi.org/10.1002/qj.2825>, 2016.
- 735 Ricard, D., Ducrocq, V., and Auger, L.: A Climatology of the Mesoscale Environment Associated with Heavily Precipitating Events over a Northwestern Mediterranean Area, *Journal of Applied Meteorology and Climatology*, 51, 468–488, <https://doi.org/10.1175/jamc-d-11-017.1>, 2012.
- Ritter, B. and Geleyn, J.-F.: A Comprehensive Radiation Scheme for Numerical Weather Prediction Models with Potential Applications in Climate Simulations, *Monthly Weather Review*, 120, 303–325, [https://doi.org/10.1175/1520-0493\(1992\)120<0303:acrsfn>2.0.co;2](https://doi.org/10.1175/1520-0493(1992)120<0303:acrsfn>2.0.co;2), 1992.
- 740 Rolph, G., Stein, A., and Stunder, B.: Real-time Environmental Applications and Display sYstem: READY, *Environmental Modelling & Software*, 95, 210–228, <https://doi.org/10.1016/j.envsoft.2017.06.025>, 2017.
- Sapiano, M. R. P. and Arkin, P. A.: An Intercomparison and Validation of High-Resolution Satellite Precipitation Estimates with 3-Hourly Gauge Data, *J. Hydrometeorol.*, 10, 149–166, <https://doi.org/10.1175/2008JHM1052.1>, 2009.
- 745 Schättler, U., Doms, G., and Schraff, C.: A Description of the Nonhydrostatic Regional COSMO-Model Part VII: User’s Guide, Deutscher Wetterdienst, P.O. Box 100465, 63004 Offenbach, Germany, 2016.
- Schiro, K. A. and Neelin, J. D.: Deep Convective Organization, Moisture Vertical Structure, and Convective Transition Using Deep-Inflow Mixing, *Journal of the Atmospheric Sciences*, 76, 965–987, <https://doi.org/10.1175/jas-d-18-0122.1>, 2019.
- 750 Schneider, M., Romero, P. M., Hase, F., Blumenstock, T., Cuevas, E., Ramos, R.: Continuous quality assessment of atmospheric water vapor measurement techniques: FTIR, Cimel, MFSR, GPS, and Vaisala RS92, *Atmos. Meas. Tech.*, 3, 323-338, <https://doi.org/10.5194/amt-3-323-2010>, 2010.
- Schraff, C. and Hess, R.: A Description of the Nonhydrostatic Regional COSMO-Model Part III: Data Assimilation, Deutscher Wetterdienst, P.O. Box 100465, 63004 Offenbach, Germany, 2012.



- 755 Schraff, C., Reich, H., Rhodin, A., Schomburg, A., Stephan, K., Perri  nez, A., and Potthast, R.: Kilometre-scale ensemble data assimilation for the COSMO model (KENDA), *Quarterly Journal of the Royal Meteorological Society*, 142, 1453–1472, <https://doi.org/10.1002/qj.2748>, 2016.
- Sherwood, S. C., Roca, R., Weckwerth, T. M., and Andronova, N. G.: Tropospheric water vapor, convection, and climate, *Reviews of Geophysics*, 48, <https://doi.org/10.1029/2009rg000301>, 2010.
- 760 Stein, A. F., Draxler, R. R., Rolph, G. D., Stunder, B. J. B., Cohen, M. D., and Ngan, F.: NOAA’s HYSPLIT Atmospheric Transport and Dispersion Modeling System, *Bull. Amer. Meteor. Soc.*, 96, 2059–2077, <https://doi.org/10.1175/BAMS-D-14-00110.1>, 2015.
- Steinke, S., Eikenberg, S., L  hnert, U., Dick, G., Klocke, D., Di Girolamo, P., and Crewell, S.: Assessment of small-scale integrated water vapour variability during HOPE, *Atmos. Chem. Phys.*, 15, 2675–2692, [https://doi.org/10.5194/acp-15-](https://doi.org/10.5194/acp-15-2675-2015)
- 765 2675-2015, 2015.
- Stevens, B.: Atmospheric Moist Convection, *Annual Review of Earth and Planetary Sciences*, 33, 605–643, <https://doi.org/10.1146/annurev.earth.33.092203.122658>, 2005.
- Th  venot, O., Bouin, M. -N., Ducrocq, V., Brossier, C. L., Nuissier, O., Pianezze, J., and Duffourg, F.: Influence of the sea state on Mediterranean heavy precipitation: A case-study from HyMeX SOP1, *Quarterly Journal of the Royal*
- 770 *Meteorological Society*, 142, 377–389, <https://doi.org/10.1002/qj.2660>, 2015.
- Tiedtke, M.: A Comprehensive Mass Flux Scheme for Cumulus Parameterization in Large-Scale Models, *Monthly Weather Review*, 117, 1779–1800, [https://doi.org/10.1175/1520-0493\(1989\)117<1779:acmfsf>2.0.co;2](https://doi.org/10.1175/1520-0493(1989)117<1779:acmfsf>2.0.co;2), 1989.
- Virman, M., Bister, M., Sinclair, V. A., J  rvinen, H., and R  is  nen, J.: A New Mechanism for the Dependence of Tropical Convection on Free-Tropospheric Humidity, *Geophysical Research Letters*, 45, 2516–2523,
- 775 <https://doi.org/10.1002/2018gl077032>, 2018.
- Wicker, L. J. and Skamarock, W. C.: Time-Splitting Methods for Elastic Models Using Forward Time Schemes, *Monthly Weather Review*, 130, 2088–2097, [https://doi.org/10.1175/1520-0493\(2002\)130<2088:tsmfem>2.0.co;2](https://doi.org/10.1175/1520-0493(2002)130<2088:tsmfem>2.0.co;2), 2002.
- Winschall, A., Sodemann, H., Pfahl, S., and Wernli, H.: How important is intensified evaporation for Mediterranean precipitation extremes?, *Journal of Geophysical Research: Atmospheres*, 119, 5240–5256,
- 780 <https://doi.org/10.1002/2013jd021175>, 2014.
- Wulfmeyer, V., Hardesty, R. M., Turner, D. D., Behrendt, A., Cadeddu, M. P., Di Girolamo, P., Schl  ssel, P., van Baelen, J., and Zus, F.: A review of the remote sensing of lower tropospheric thermodynamic profiles and its indispensable role for the understanding and the simulation of water and energy cycles, *Reviews of Geophysics*, 53, 819–895, <https://doi.org/10.1002/2014rg000476>, 2015.
- 785 Xoplaki, E., Trigo, R. M., Garc  ndez, R., Kuglitsch, F. G., Mariotti, A., Nieto, R., Pinto, J. G., Pozo-V  zquez, D., Saaroni, H., Toreti, A., Trigo, I. F., Vicente-Serrano, S. M., Yiou, P., and Ziv, B.: Large-Scale Atmospheric Circulation Driving

Extreme Climate Events in the Mediterranean and its Related Impacts, in: The Climate of the Mediterranean Region, Elsevier, 347–417, <https://doi.org/10.1016/b978-0-12-416042-2.00006-9>, 2012.

790

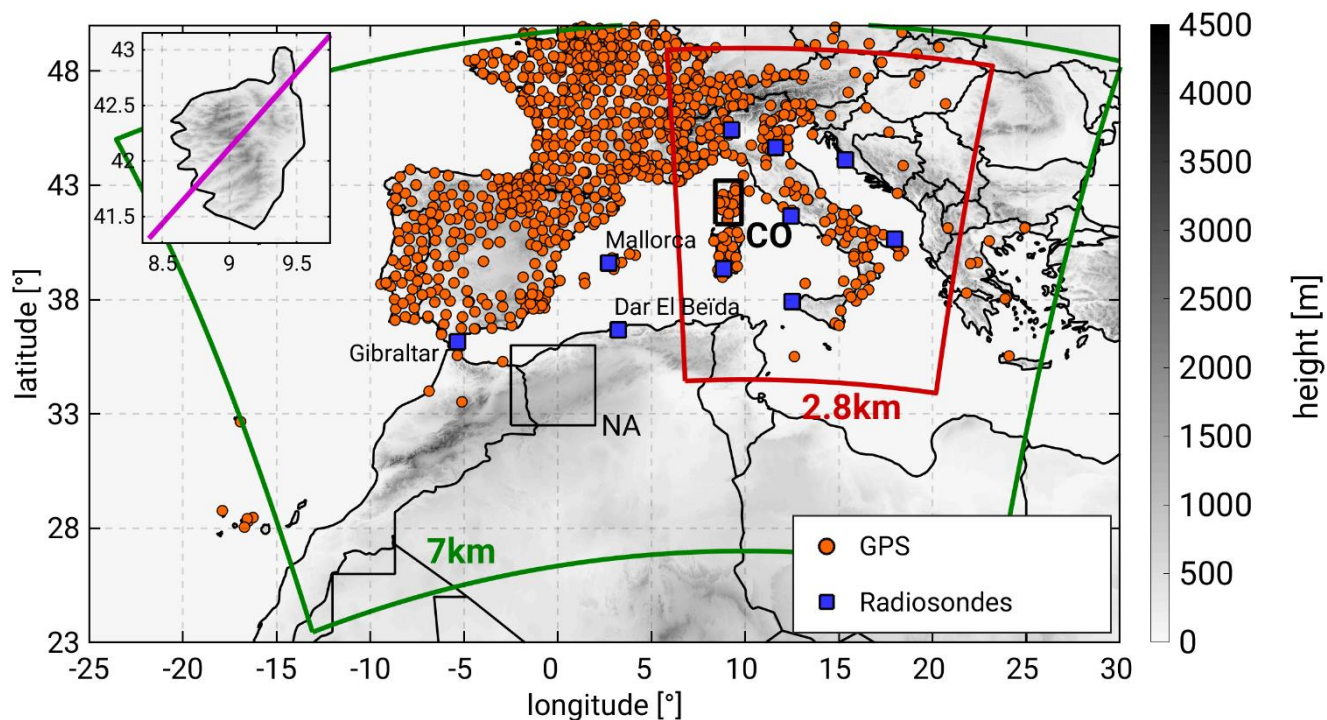
795

800

805 **Table 1. Mean Absolute Error (MAE), Agreement Index (AI), and Mean Bias (MB) of IWV between the model and the observations. The selected observations are all radiosondes available in the period 26-Oct 0000 UTC to 28-OCT 0000 UTC at the 7 stations within the 2.8 km simulation domain (see red box in Fig. 1). All model values have been interpolated to the location of the radiosonde station from the nearest neighbours. The difference between model and station height never exceeded 30 m.**

Rads vs. COSMO-CLM (IWV)	MAE [mm]	AI	MB [mm]
CTRL-7	2.7	0.88	0.61
NDG-7	2	0.93	-0.04
CTRL-2.8	2.7	0.89	0.38
NDG-2.8	2	0.92	-0.08

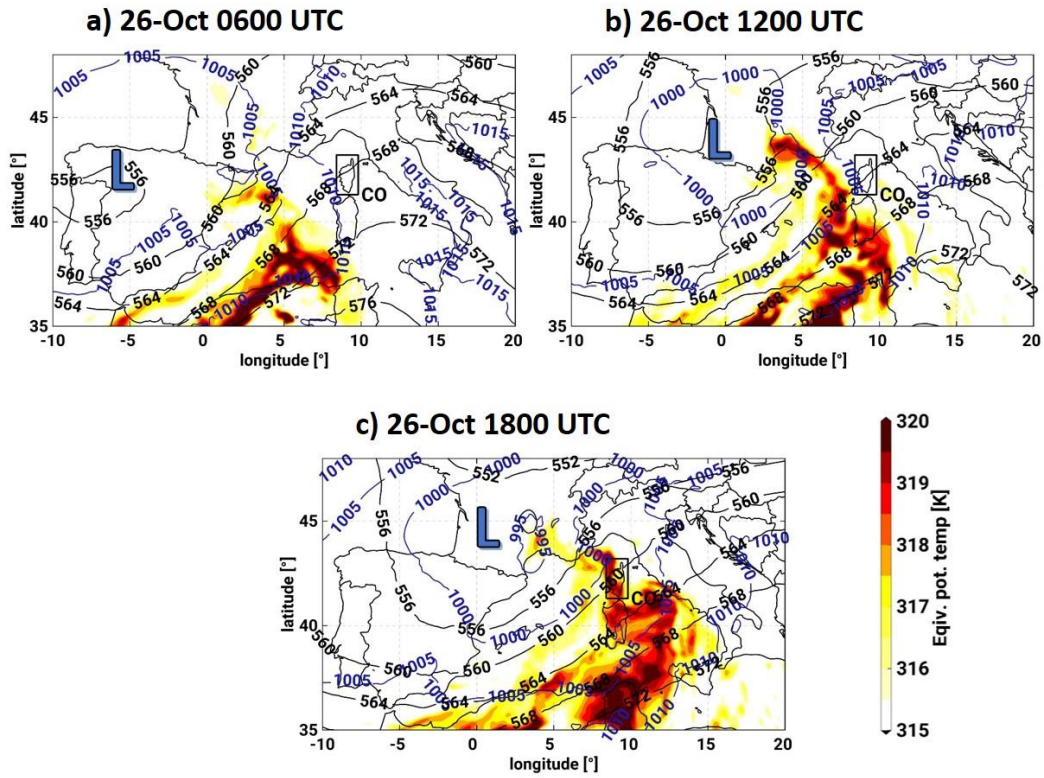
810



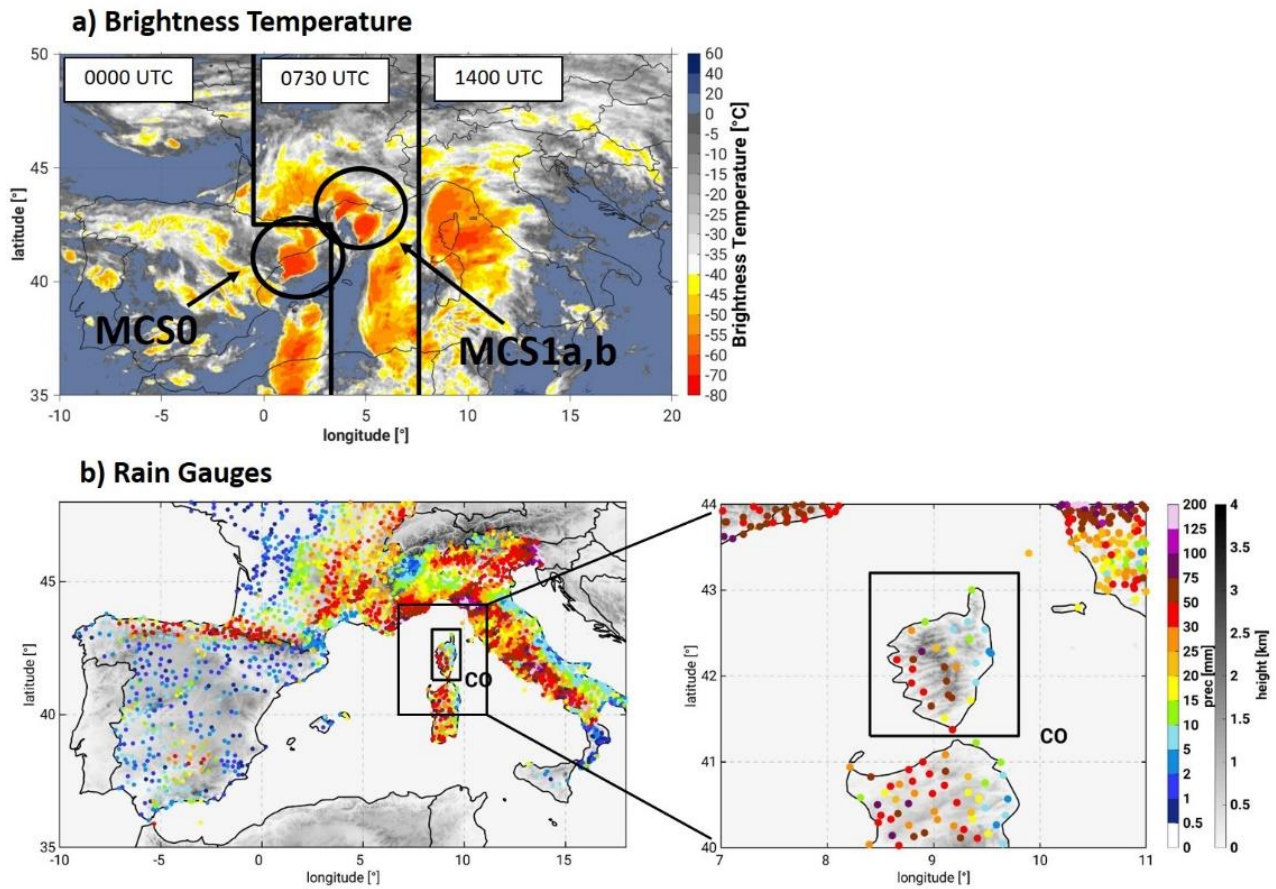
815

Figure 1: Simulation domains for the CTRL-7 and NDG-7 runs (green line) and for the CTRL-2.8 and NDG-2.8 (red line). The investigation area CO is depicted by the thick lined black box. The box over North Africa (NA) denotes the region of intense evapotranspiration between 20-Oct and 27-Oct (see Sect. 4.1). The orange scatter points show the location of the GPS receivers used for nudging and the blue squares the location of the radiosondes used for validation and process-understanding. The upper left corner shows a detail of the orography over CO with a purple transect used for representation of the humidity vertical distribution in Fig. 5.

820

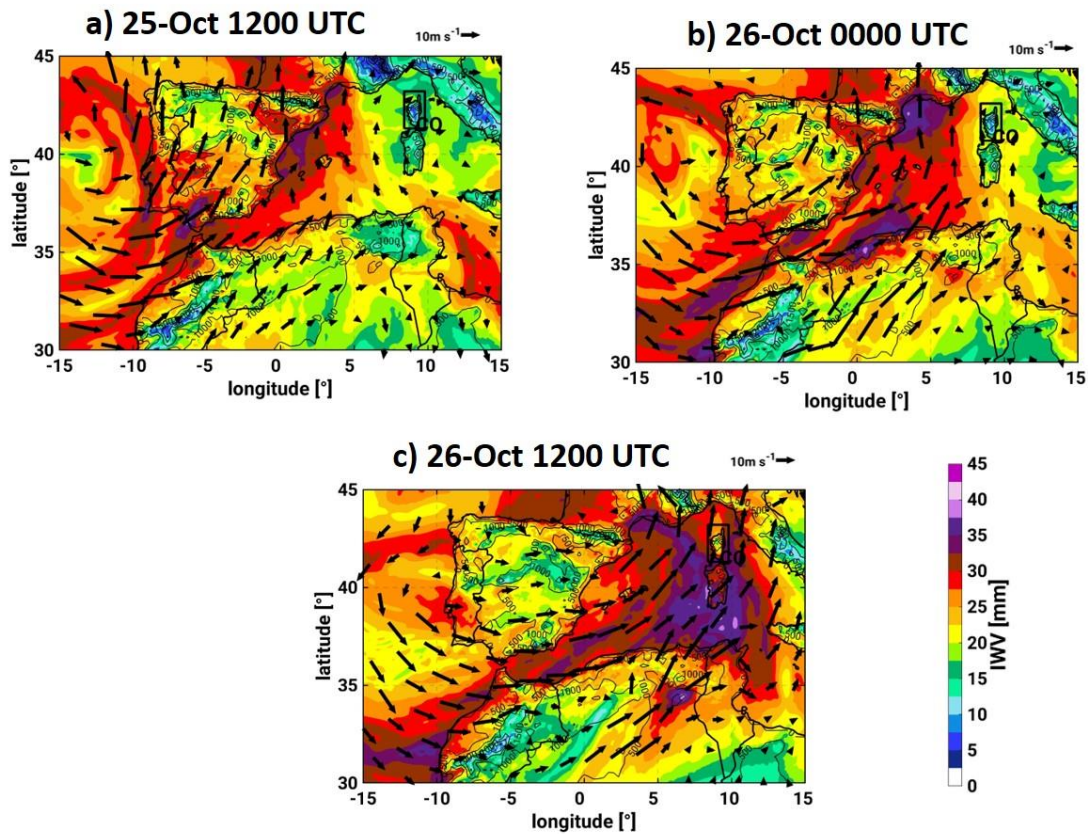


825 **Figure 2. CTRL-7 simulation of 500 hPa geopotential height in black isolines (gpdam), mean sea-level pressure in blue isolines (hPa) and equivalent potential temperature at 850 hPa in colour scale (K) on the 26-Oct-2012 at 0600 UTC (a), 1200 UTC (b) and 1800 UTC (c).**

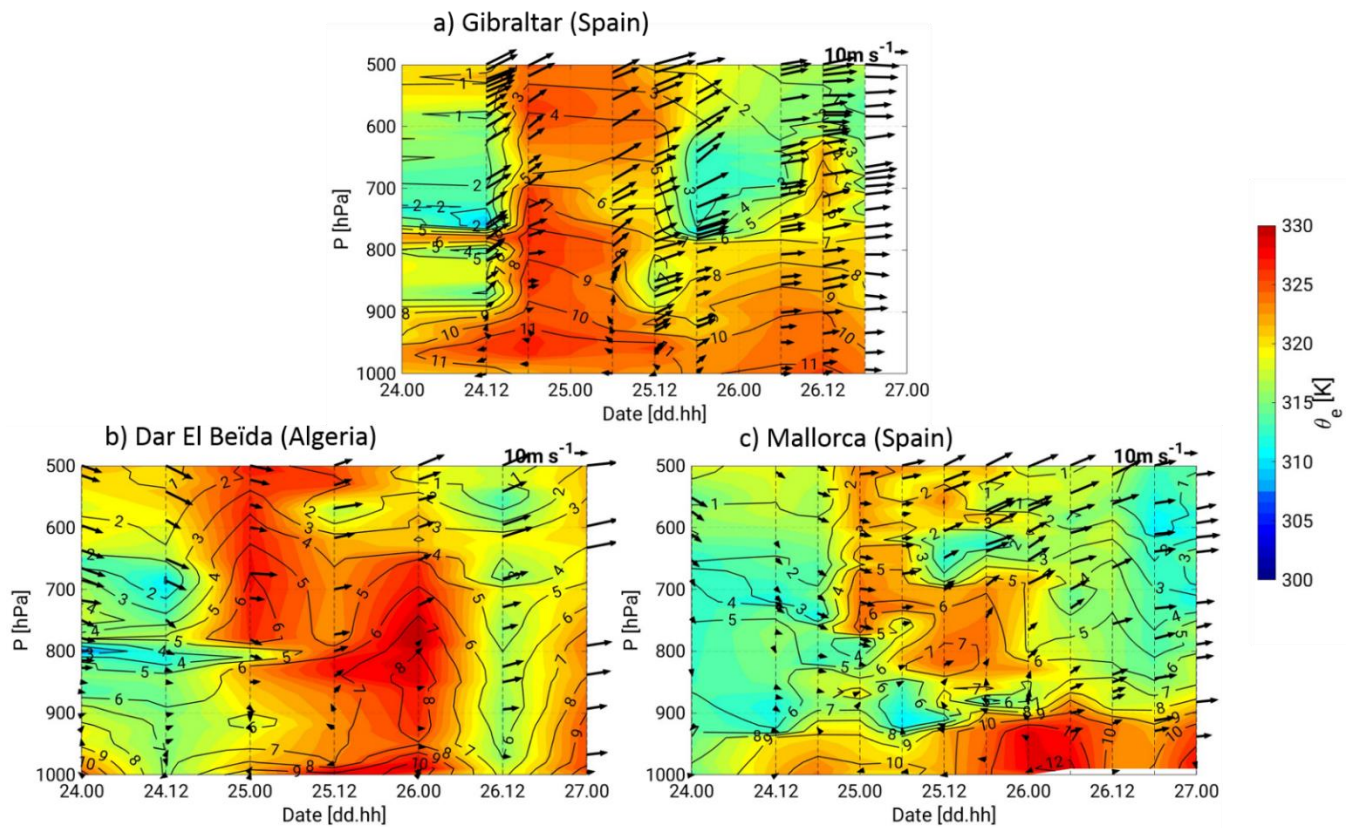


830 **Figure 3. Composite image of brightness temperature as measured by the SEVIRI instrument on the 26-Oct-2012, at 0000 UTC, at 0730 UTC and at 1400 UTC (a). Rain gauge accumulated precipitation over the complete WMed region between 26-Oct 1300 UTC and 27-Oct 1500 UTC and zoomed over the study region of Corsica (b). The accumulation period shown is the period of heavy precipitation over our main study region, the island of Corsica (black box), during this event.**



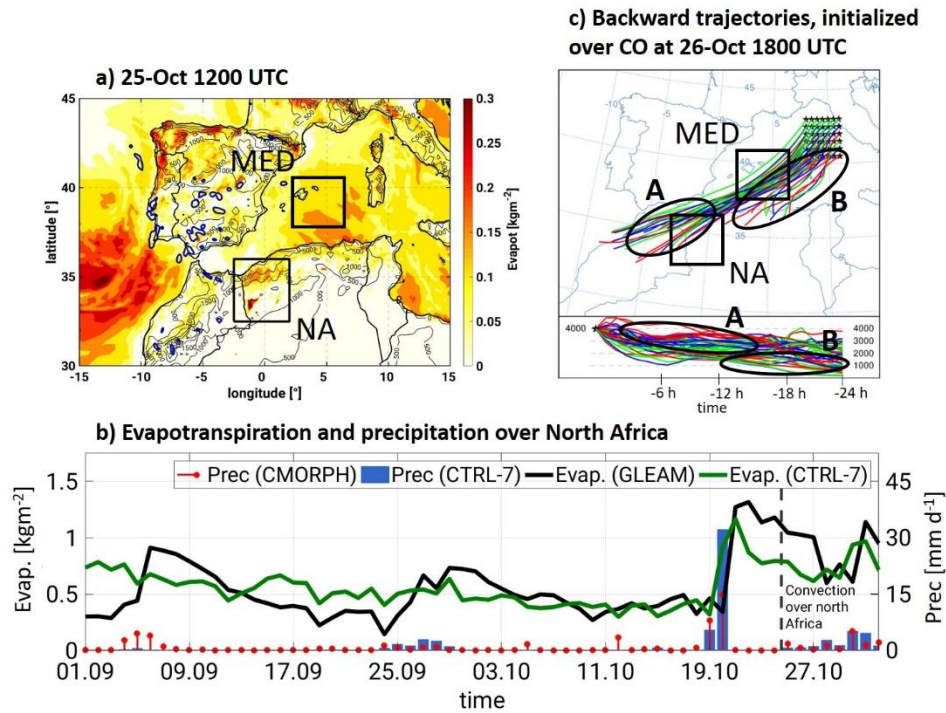


835 Figure 4. Spatial distribution of IWB and winds at 850 hPa as represented by CTRL-7 on the 25-Oct-2012 at 1200UTC (a), 26-Oct-2012 at 0000UTC (b) and on the 26-Oct-2012 at 1200UTC (c).



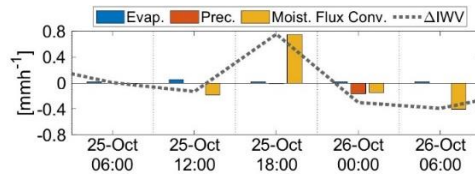
840 **Figure 5. Height-time cross-sections at Gibraltar (a), Dar el Beïda (b) and Mallorca (c) between 24-Oct 0000UTC and 27-Oct 0000UTC. The colour shading stands for Equivalent Potential Temperature ( $\theta_e$ ), the contours denote specific humidity and the arrows show the direction and speed of horizontal wind at the stations. The location of the radiosondes can be seen in Fig. 1.**



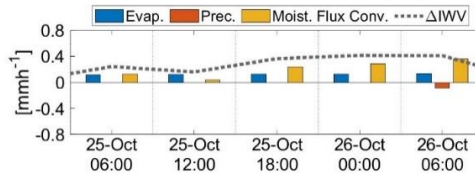


845 Figure 6. Spatial distribution of evapotranspiration (colour shading) and vertical updrafts with vertical wind speeds larger than 0.25  
 ms<sup>-1</sup> (blue contours) simulated with CTRL-7 on the 25-Oct at 1200UTC (a). The black boxes denote the regions of intense  
 evaporation. (b) Spatially averaged daily evapotranspiration (GLEAM and CTRL-7) and daily precipitation (CMORPH and CTRL-  
 7) over north Africa (black box) between 01-Sep-2012 and 02-Nov-2012. The CTRL-7 precipitation has been upscaled to the coarser  
 850 grid of CMORPH (0.0727°). Likewise, CTRL-7 evapotranspiration has been upscaled to the coarser grid of GLEAM of 0.25 °. (c)  
 Lagrangian backward trajectories obtained with the HYSPLIT model, starting on the 26-Oct-2012 1800 UTC (initiation of the event  
 over Corsica) back to for 24 h.

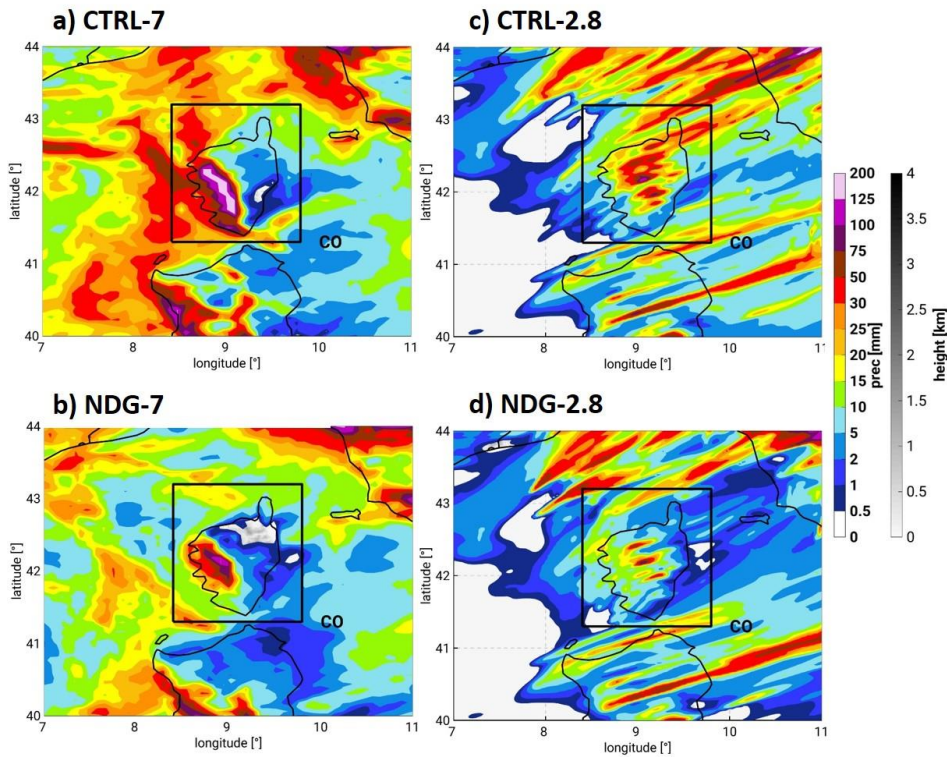
a)



b)



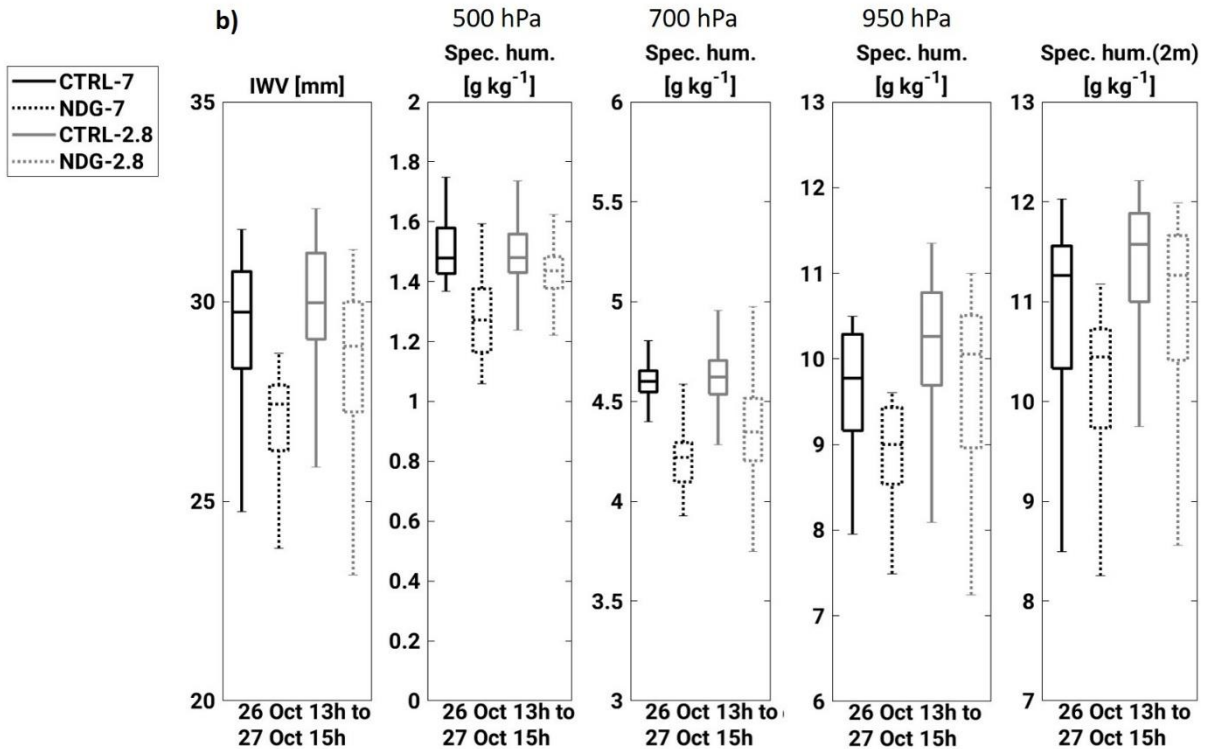
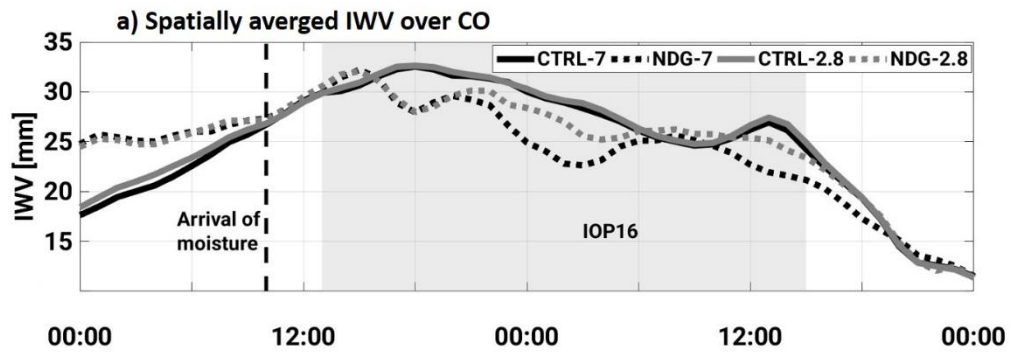
855 **Figure 7. Temporal evolution of the moisture budget terms, variation of IWV ( $\Delta$ IWV), Moisture Flux Convergence, Evapotranspiration and Precipitation. Hourly values are given. The spatial averages are performed over the investigation areas NA (a) and MED (b). The values are obtained from CTRL-7.**



860 **Figure 8. COSMO-CLM accumulated precipitation over Corsica between 26-Oct 1300 UTC and 27-Oct 1500 UTC i.e. during the period of precipitation over the island.**

865 **Table 2. Model precipitation validation against Rain Gauges (RG). COSMO-CLM has been interpolated to the location of the RG for the first three metrics Root Mean Square Error (RMSE), hourly standard deviation difference ( $OBS_{\sigma} - MOD_{\sigma}$ ) and spatially averaged differences ( $\overline{OBS} - \overline{MOD}$ ). On the contrary, all precipitation values simulated by COSMO-CLM over the island of Corsica are used in the last two metrics, standard deviation difference ( $OBS_{\sigma} - MOD_{\sigma}$ ) and difference of maximum precipitation ( $OBS_{max} - MOD_{max}$ ). The temporal resolution of each metric is given in brackets. The description of the validation metrics can be found in the Annex.**

[mm]	Interp. To RG location			Distributions without interpolation	
	RMSE (1h)	$OBS_{\sigma} - MOD_{\sigma}$ (1h)	$\overline{OBS} - \overline{MOD}$ (27h)	$OBS_{\sigma} - MOD_{\sigma}$ (27h)	$OBS_{max} - MOD_{max}$ (27h)
CTRL-7-Init1Sep	3.1	-0.35	-10.4	-32	-185
NDG-7- Init1Sep	2.6	1.07	15.4	-0.7	-58
CTRL-2.8-Init1Sep	3.1	0.55	14.6	6	-3
NDG-2.8-Init1Sep	2.7	1.03	21.5	12	11



870 Figure 9. Spatially averaged IWP for all simulations during the event. The area for averaging is shown in Fig. 1 (CO) and the model output has been upscaled to a common coarser grid. The period shown is 26-Oct 0000 UTC to 28-Oct 0000 UTC. (b) Box and whiskers plots showing the median, the percentiles 25 and 75 and the extreme values of IWP and specific humidity at 500 hPa, 700 hPa, 950 hPa and at 2m height. All box and whiskers are obtained from the distribution of values for the shown quantities between the 26-Oct 1300 UTC and 27-Oct 1500 UTC over the study region CO.

875

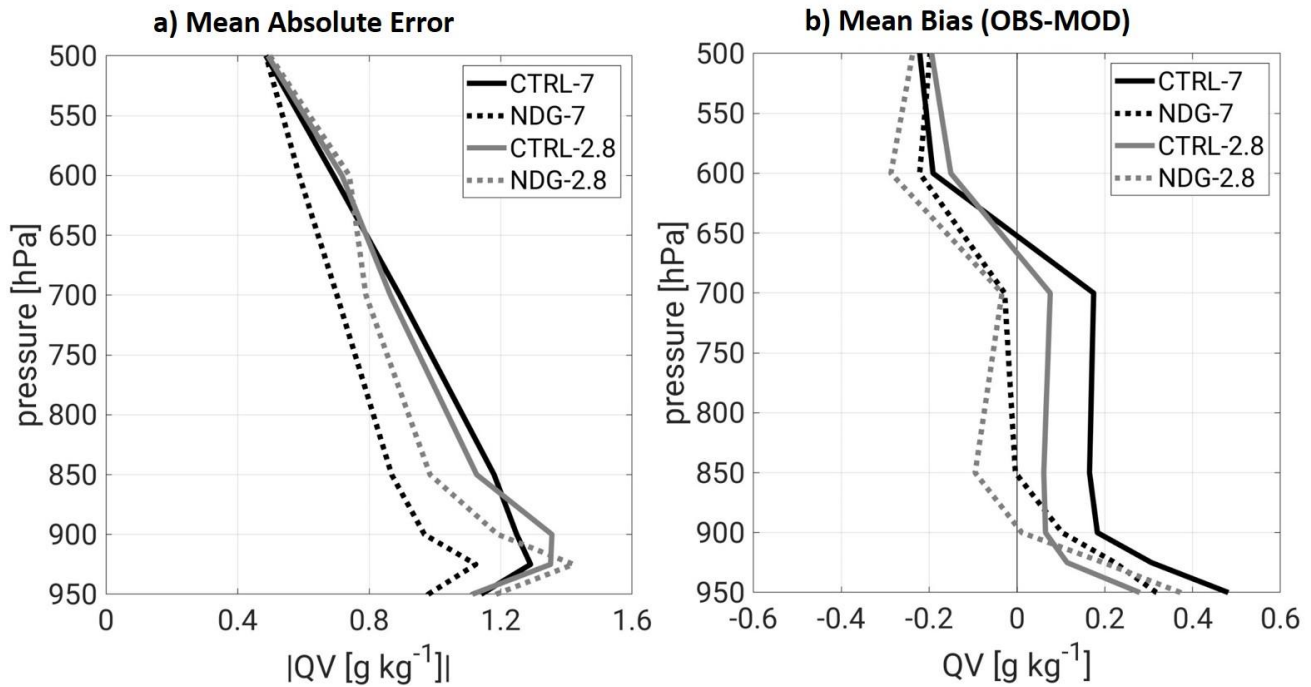
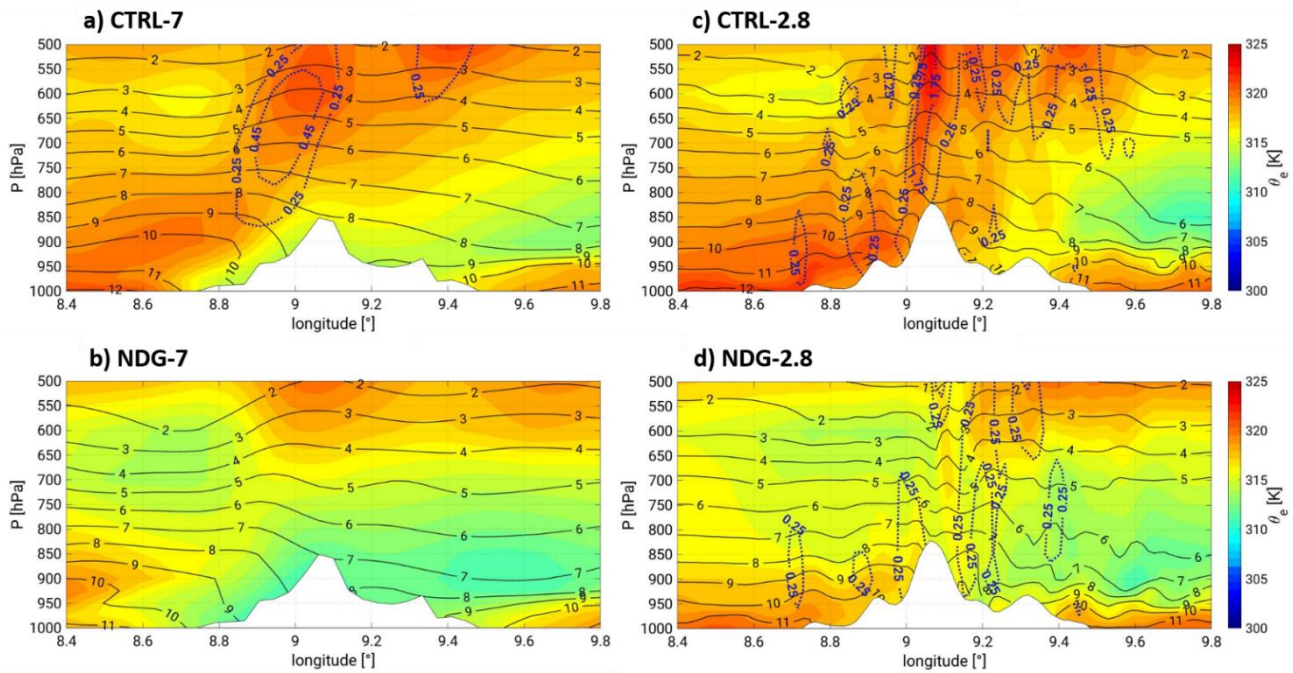


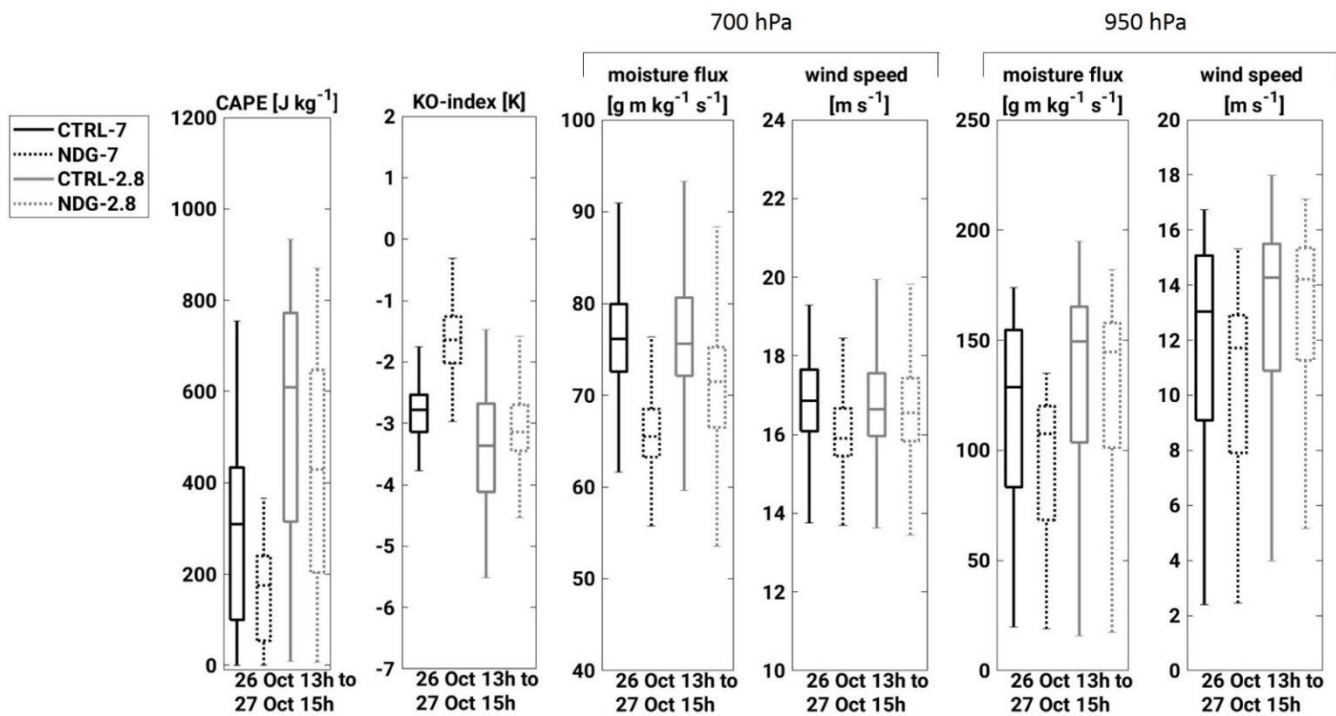
Figure 10. Validation of the model representation of the vertical distribution of specific humidity quantified by the Mean Absolute Error (a) and the Mean Bias as the OBS-MOD (b). All model values are validated against the radiosondes available in the period 26-Oct 0000 UTC to 28-OCT 0000 UTC at the 7 stations within the 2.8 km simulation domain (see red box in Fig. 1). All model values have been interpolated to the location of the radiosonde station from the nearest neighbours and the vertical specific humidity values have been interpolated to eleven pressure levels between 950 and 500 hPa. No values are shown below 950 hPa given the lack of available data for several stations below this level.

880

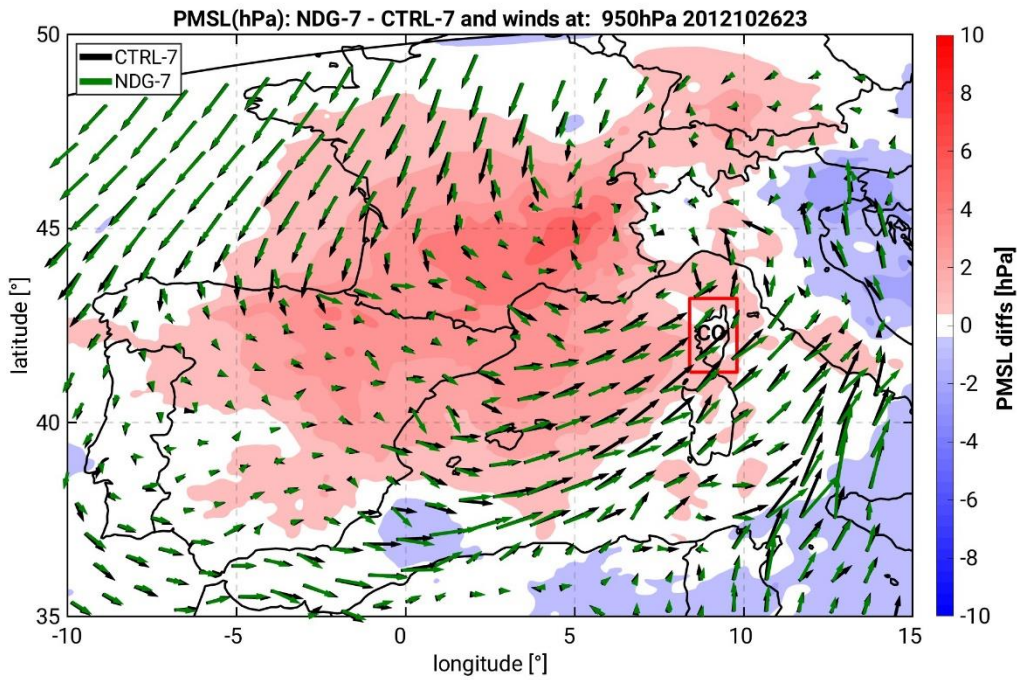


885 **Figure 11.** Vertical cross sections along the mean wind direction between 700 hPa and 1000 hPa (see transect in Fig. 1) on the 26-Oct 1700UTC. The selected hour corresponds to the first precipitation maximum represented over Corsica by the COSMO-CLM simulations. The position of the transect is represented in Fig. 1. The specific humidity values are represented as black contour lines, the colour shading represents equivalent potential temperature ( $\theta_e$ ). Vertical windspeed is represented in blue dashed contours, where isolines start at 0.25 m/s.





890 Figure 12. Box and whiskers plots showing the median, the percentiles 25 and 75 and the extreme values of CAPE, KO-index, moisture flux and horizontal wind speeds. All box and whiskers are obtained from the distribution of values for the shown quantities between the 26-Oct 1300 UTC and 27-Oct 1500 UTC over the study region CO.



895 **Figure 13.** Spatial distribution of the differences in Pressure at the Mean Sea Level (PMSL) between NDG-7 and CTRL-7 on the 26-Oct 2300 UTC. Red colours indicate larger PMSL in NDG-7. Horizontal winds at 950 hPa are represented by black (CTRL-7) and green (NDG-7) arrows.



**Table 3. Metrics for precipitation validation for the additional simulations initialized on the 20-Oct-2012. A description of the used metrics can be found in the Annex.**

[mm]	Interp. To RG location			Distributions without interpolation	
	<b>RMSE</b> (1h)	<b><math>OBS_{\sigma} - MOD_{\sigma}</math></b> (1h)	<b><math>\overline{OBS} - \overline{MOD}</math></b> (27h)	<b><math>OBS_{\sigma} - MOD_{\sigma}</math></b> (27h)	<b><math>OBS_{max} - MOD_{max}</math></b> (27h)
CTRL-7	3.3	-0.85	-19.1	-33	-170
NDG-7	2.5	0.73	12.5	-5	-79
NDG-7-1h	2.5	0.95	12.2	-4	-50
CTRL-2.8	3.6	-0.15	9.5	-3	-74
NDG-2.8	2.6	1.64	23.8	11	-16
NDG-2.8-1h	2.5	1.64	23.6	10	-17

### 13. Annex

905

**Table A.1** Precipitation validation metrics used in Tables 2 and 3.  $N$  are the total numbers of measurements at the rain gauges stations, hourly (1 h) or accumulated (27 h).  $M$  are all model grid points over land. For the first two metrics all hourly values between 26-Oct 1300 UTC and 27-Oct 1500 UTC are considered and COSMO-CLM is interpolated to the station's location. The third metric is an average of accumulated precipitation with COSMO-CLM values interpolated to the station's location. The last two metrics considered all observed and simulated precipitation values over land.

	Formula
<b>RMSE</b> (1h)	$\sqrt{\sum_{i(1h)}^N ((OBS_i - \overline{OBS}) - (MOD_i - \overline{MOD}))^2}$
<b><math>OBS_\sigma - MOD_\sigma</math></b> (1h)	$\sqrt{\frac{1}{N} \sum_{i(1h)}^N (OBS_i - \overline{OBS})^2} - \sqrt{\frac{1}{N} \sum_{i(1h)}^N (MOD_i - \overline{MOD})^2}$
<b><math>\overline{OBS} - \overline{MOD}</math></b> (27h)	$\frac{1}{N} \sum_{i(27h)}^N OBS_i - \frac{1}{N} \sum_{i(27h)}^N MOD_i$
<b><math>OBS_\sigma - MOD_\sigma</math></b> (27h)	$\sqrt{\frac{1}{N} \sum_{i(27h)}^N (OBS_i - \overline{OBS})^2} - \sqrt{\frac{1}{M} \sum_{j(27h)}^M (MOD_j - \overline{MOD})^2}$
<b><math>OBS_{max} - MOD_{max}</math></b> (27h)	$\max(OBS_{i(27h)}) - \max(MOD_{j(27h)})$

910 **Table A.2** IWV Validation metrics used in Table 1 and Fig. 10 in Section 4.2

	Formula
Absolute Error (MAE)	$\frac{1}{N} \sum_{i=1}^n  obs_i - mod_i $
Mean Bias (MB)	$\frac{1}{N} \sum_{i=1}^n (obs_i - mod_i)$
Agreement Index (AI)	$1 - \frac{\sum_{i=1}^n (obs_i - mod_i)^2}{\sum_{i=1}^n ( obs_i - \overline{obs}  +  mod_i - \overline{mod} )^2}$